38p

NASA CONTRACTOR REPORT

NASA CR-69

DEPLOYABLE CENTRIFUGALLY STABILIZED STRUCTURES FOR ATMOSPHERIC ENTRY FROM SPACE

by H. U. Schuerch and R. MacNeal

Prepared under Contract No. NASw-652 *by*
ASTRO RESEARCH CORPORATION
Santa Barbara, California
for

NATIONAL AERONAUTICS AND SPACE ADMINISTRATION • WASHINGTON, D. C. • JULY 1964

DEPLOYABLE CENTRIFUGALLY STABILIZED STRUCTURES FOR ATMOSPHERIC ENTRY FROM SPACE

By H. U. Schuerch and R. MacNeal

Prepared under Contract No. NASw-652 by
ASTRO RESEARCH CORPORATION
Santa Barbara, California

NATIONAL AERONAUTICS AND SPACE ADMINISTRATION

For sale by the Office of Technical Services, Department of Commerce,
Washington, D.C. 20230 -- Price $1.00

INDEX

SUMMARY

n 3690

PART I

A number of structural and aerodynamic concepts for centrifugally deployed variable geometry atmospheric entry aids are discussed. These include means for controlling apex angle of centrifugally stabilized conical flight bodies, the concept of isothermal flight, i.e., atmospheric entry at constant surface temperature, and analytical design of optimum rotor blade structures. Materials for flexible rotor construction are reviewed and classified according to a temperature-strength parameter that is characteristic for the intended application. Several aerodynamic rotor models subject to qualitative tests are described. An application of the entry rotor concept to a Mars and Earth landing capsule is presented in the form of a conceptual design configuration.

PART II

Expressions for the aerodynamic forces on a rotor blade element are developed using the Newtonian momentum concept and are applied to the problem of producing lift as well as drag during atmospheric entry. The relative merits of cyclic blade pitch, cyclic changes in effective blade area, and tip flapping vanes as trim control devices in lifting flight are discussed.

Lateral stability in axial flight is investigated using rotor derivatives evaluated from a consideration of the dynamic equations of a flapping rotor blade with offset flap hinge. The effects of large coning angles and rotor cross-derivatives are included. Calculations for points along typical reentry trajectories indicate that a rotary wing reentry vehicle possesses an inherent tendency toward a mild instability similar to that of hovering subsonic helicopter. Means for eliminating the instability are discussed.

author

PART I

CONCEPTS OF ROTARY WING ATMOSPHERIC ENTRY

Introduction

Atmospheric entry and planetary landing of spacecraft are usually considered in view of fixed geometry flight configurations, and of vehicles with relatively high (>> 1 psf) "ballistic parameters" (Ref. 1). These configurations have emerged from development of ballistic missiles which, in many respects, are the forerunners of the current generation of space vehicles.

In recent years, several studies of deployable and variable geometry configurations have been conducted, including inflatable wings, paragliders, variable drag brakes and "rotochutes" (Ref. 2-5). These allow the deployment of relatively large and lightweight lift and drag surfaces for aerodynamic control of atmospheric entry without being limited by the requirements for compactness which are imposed by the available booster payload compartment size.

Several operational advantages can be derived from deployable and variable geometry configurations:

- The possibility of low ballistic parameters (≤ 1psf) materially reduces heating rates and prolongs flight time, thus it simplifies both heat protection and flight path control aspects of manned atmospheric entry.

- The concept of a variable geometry configuration adds a means of control for selection of survivable entry trajectories from those initial entry conditions (hyperbolic velocities and steep entry angles) which would be catastrophic for fixed geometry vehicles.

Studies of variable geometry and filamentary structures in space operations (Ref. 6-8) indicate the merits of centrifugal stabilization mechanisms for deployable surface structures.

This first portion of the paper summarizes some of the aerodynamic and structural concepts that have been developed in the course of an initial, exploratory study of rotary atmospheric entry aids.

A. Variable Geometry Rotors

The basic configuration selected for study is that of a circular cone with variable apex angle, rotating about its axis. This configuration is relatively simple in its aerodynamic and structural characteristics. The structure is considered to be made from thin, flexible material, resistant only in tension. The aerodynamic contour is to be stabilized and controlled by interactions of aerodynamic and inertial forces. Packaging of the structure into a compact pre-entry configuration is to be accomplished by folding of the continuously flexible structure.

Three principally different mechanisms of apex angle variation as shown schematically in Figure 1a-c have been considered:

- The basic cone may be slit along several meridional lines. This converts the cone into a leaved disk, generic of the well known helicopter rotor with hinged blades. The "solidity" of the rotor disk and the particular planform shape of each "leaf" will determine the coning angle at which overlap of the individual blades occurs and at which the rotor converts aerodynamically again to a cone. Variable coning angle requires compliance of the material only at the apex or "hub" of the rotor and may be effected by localized flapping hinges.

- The basic cone may be considered as modified by meridional or near-meridional corrugations. The depth of the corrugation increases as the cone becomes more acute, it decreases to zero into the configuration where the structure forms a smooth right circular cone or, in the limit, a flat disk. The material of construction for this type of deformation needs to be compliant in bending but may be inextensible in its own plane. The mechanism of deformation is one of metric and topological invariance (isometry) since no in-plane strains nor cuts are required to allow the geometrical deformation (Ref. 8). Bending compliance of the structure is required along meridional lines in circumferential direction only.

- A variable apex cone may be generated by a fabric material that allows a "trellis shear" deformation. Here the condition of isometry for the deformed surface is relaxed, since the material is considered as inextensible only along two specified directions, namely, in the directions of two families of threads or filaments. A study of the deformation kinematics of fabric cones shows, that a thread geometry forming two counter-rotating sets of logarithmic spirals emanating from the hub will yield the desired apex angle variability of a continuous cone shaped struc-

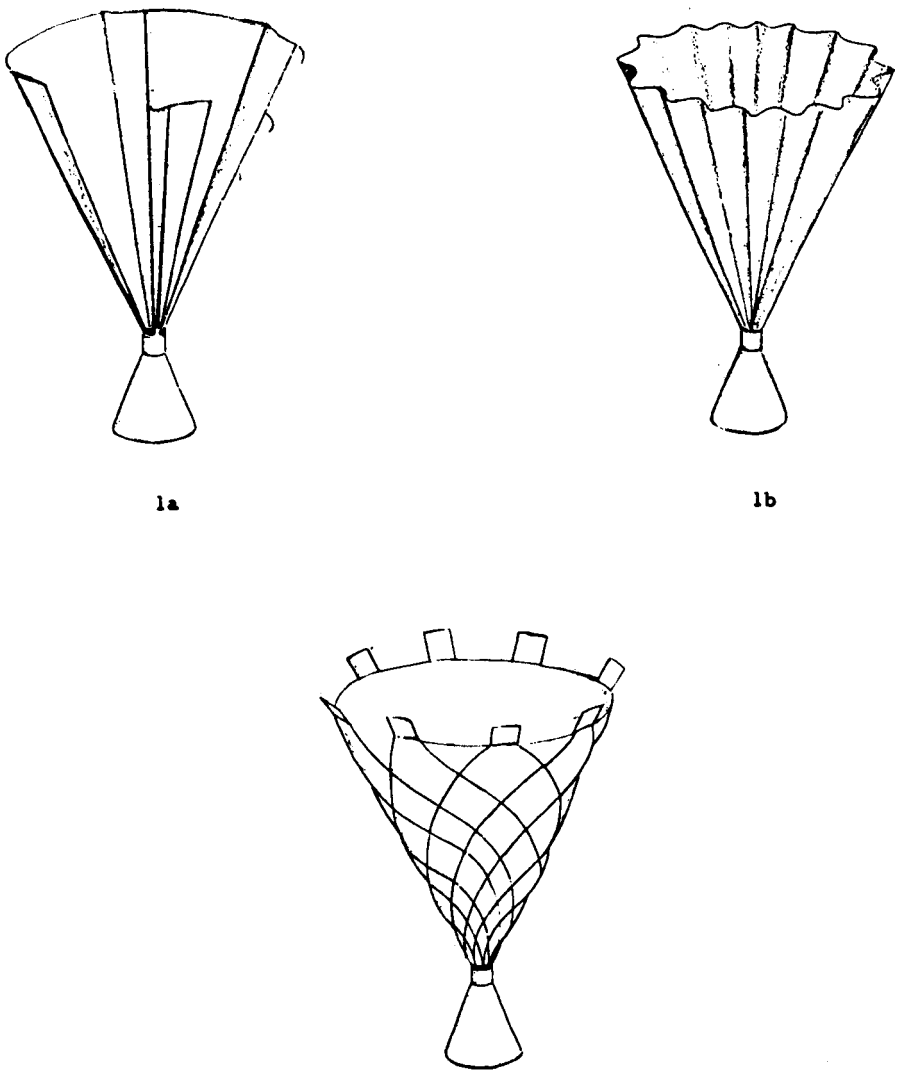

1a 1b

1c

Figure 1. Variable Geometry Rotor Configurations.

ture. For this design, a change in coning angle of the structure is associated with a uniform change in the angles formed between the two sets of spirals.

B. Isothermal Atmospheric Entry

From the discussion of variable geometry rotor configurations in the previous paragraph, it is clear that the structures considered will be essentially thin walled flexible membranes made from thin films, fabrics or thin fiber laminates. These will be incapable of storing appreciable amounts of heat, and probably prove impractical for application of artificial or ablation cooling

methods. Furthermore, the entry flight duration may be expected to be long, the total heat input large and the heating rates relatively low. These structures, therefore, will operate essentially at equilibrium temperature during the significant portions of the entry deceleration, requiring that the input of aerodynamic heating to the vehicle surface must equal the heat radiated from the surface to the environment.

Assuming that the materials of construction will be capable to operate at a given maximum absolute temperature, θ, it appears that an "optimum braking trajectory" can be defined for which this temperature is uniform throughout the surface and constant throughout the significant portions of the atmospheric flight path. A vehicle operation which satisfies these conditions of uniform and constant surface temperature will be designated as Isothermal atmospheric entry.

To define the conditions of configurational and flight path control required to achieve isothermal flight, consider a vehicle in unpowered flight through the atmosphere of a stationary planet. The forces acting on the vehicle and the notations used are shown in Figure 2.

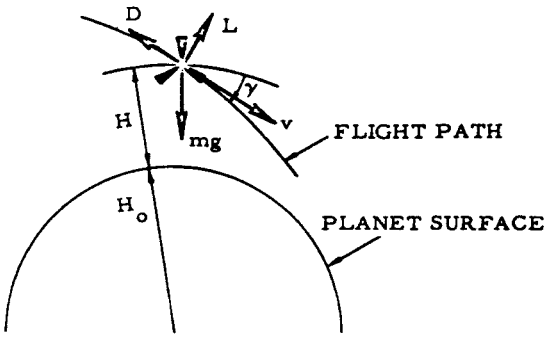

Figure 2. Atmospheric Entry Forces.

Considering equilibrium in directions tangential and normal to the flight path yields, respectively

$$m \frac{dv}{dt} - mg \sin\gamma + D = 0 \qquad (1)$$

$$mv \frac{d\gamma}{dt} - mg \cos\gamma + L + \frac{v^2}{H+H_o} \cos\gamma = 0 \qquad (2)$$

Eq. (1) can be written in terms of energy rates as follows:

$$\frac{d}{dt}\left(\frac{mv^2}{2}\right) + g \frac{dH}{dt} + Dv = 0 \qquad (1a)$$

The third term in eq. (1a) describes the rate at which energy is lost by dissipation. A portion of this power will be transferred to the vehicle in the form of heat, the remainder will appear in the wake as turbulence and heat.

Following Gazley's notation (Ref. 1), the heat transferred to the vehicle is expressed as a fraction, f, of the total energy dissipation. For a given body geometry, f is a function of altitude, as shown in Figure 3, which is reproduced from Reference 1. Note that for altitudes where free molecular flow exists, the fraction f assumes a value of .5, i.e., half of the dissipated energy is transferred to the vehicle, the other half is transferred to the wake (equipartition). For equilibrium, the rate at which energy is transmitted to the vehicle must equal the rate at which it is radiated from the surface, thus

$$Dvf = \sigma \epsilon \theta^4 A (VF) \qquad (3)$$

where

σ is the Boltzman constant

ϵ is the surface emissivity

θ is the absolute surface temperature

A is the surface area of the vehicle, and

(VF) is a "view factor" that relates the effective radiating surface to the vehicle surface.

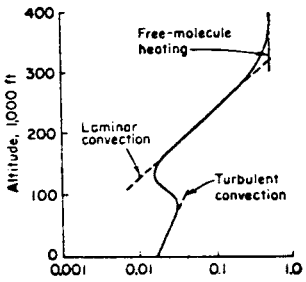

Figure 3. Energy Conversion Fraction.

For an obtuse, cone, approaching a flat disk, (VF) will approach a value of 2, since both sides of the thin structure will be at the same temperature and will radiate off energy, while only the frontal side is subject to heat input.

Substituting eq. (3) into eq. (1) and regrouping yields:

$$\frac{dv}{dt}\Big/g - \sin\gamma = \frac{v^*}{v} \frac{g_o^*}{fg} \qquad (1b)$$

where g_o^* is a reference gravitational acceleration

of 32.2 ft/sec^2 (earth surface) and

$$v^* = \frac{\sigma \epsilon \theta^4 (VF)}{g^{\frac{1}{2}} m/_A}$$

is a specific velocity, characteristic for the vehicle's ability to decelerate by rejecting energy from a given area A with a view factor (VF) at an absolute surface temperature θ.

Eq. (1b) and (2) may be integrated for any given initial condition and lift program provided that f and g are known functions of altitude H, and provided that (VF) is known. This allows to establish generalized isothermal trajectory plots. From these the control demands can be derived in terms of drag and/or lift requirements for specific atmospheric density variations. Two simple cases have been considered in some detail: Zero lift, pure drag modulation; and constant drag area, pure lift modulation:

Drag Modulation

Drag modulation can be accomplished by adjusting the coning angle, β, measured between the plane normal to the cone axis and the cone meridian ("Helicopter-coning angle"). This controls the frontal area to provide the required drag at the instantaneous velocity and altitude. A simple means of control for β consists in a rotor speed control device which provides the required centrifugal force components to equilibrate the coning moments resulting from aerodynamic pressure forces and axial rotor inertia forces.

For the purpose of this exploratory study, it was assumed that the view factor (VF) be unity, and the surface emissivity equal .9. The vehicle will deploy the cone at a given initial altitude, velocity, v_o, and flight path angle, γ_o, into essentially a flat disk. The trajectory is then computed for this fixed drag geometry, until the desired absolute surface equilibrium temperature θ is reached. At this point, the coning angle control is assumed to become effective, such that the subsequent portion of the trajectory becomes isothermal. After deceleration to a low velocity, the coning angle required to maintain isothermal flight decreases again to zero. Finally, a constant area configuration may again be assumed for terminal flight at subsonic equilibrium glide velocity.

The drag is assumed to be a function of flight velocity, v, atmospheric density, ρ_{ATM}, coning angle β and cone surface area A as follows:

$$D = A \rho_{ATM} v^2 \cos^3 \beta \qquad (4)$$

"U. S. Standard Atmosphere, 1962" was used for earth atmospheric data (Ref. 12), exponential density-altitude variations have been assumed for Venus and Mars atmospheres with numerical values for sea level density and exponential coefficients taken from Reference 1. The energy fraction f, was adapted to Venus and Mars by assuming f to be dependent on atmospheric density only.

A number of typical entry trajectories for Earth, Venus and Mars are shown on Figures 4-6. These were selected for entry conditions varying from circular orbit decay to straight-in entry with parabolic velocity and with specific velocities ranging from 20,000 to 80,000 ft/sec. The isothermal and terminal portions of the flight are shown as a solid line. The initial flight phases, where the surface temperature is lower than the maximum permitted by the design, are shown as dotted lines. Note that the "high v*" Mars trajectories never become isothermal, i.e., the cone will remain fully deployed as a flat disk throughout the trajectory, and the vehicle's operation is not temperature limited.

Several restrictions will occur in practice for specific applications. These involve the coning angle requirement which is subject to practical limitations. Also, for coning angles higher than 45° the underlying assumptions for drag and heat transfer would need to be modified. Finally, for manned operation, the permissible trajectory deceleration needs to be limited to a value somewhat below 10 Earth g's. In practice, the drag area control mode would need to be adapted to stay within those limits and the practicality of the individual trajectory will have to be assessed in view of these limitations.

Lift Modulation

Lift modulation can be accomplished in trimmed flight by variation of incidence angles between rotor axis and flight path. Means of accomplishing trim at finite angles of attack are discussed in Part II of this paper. For the purpose of trajectory analysis, it was assumed that the coning angle and drag would remain constant. Isothermal flight is then achieved by holding altitude at which the desired equilibrium temperature is reached until the vehicle decelerates sufficiently to allow descent into denser atmospheric strata. This defines the flight path angle γ in function of altitude. The required lift, then can be obtained from eq. (2). It is assumed that the vehicle enters the atmosphere tangentially, i.e., at a flight path angle of essentially zero. The relation between flight velocity, flight path angle and required lift vs altitude on earth entry are shown in Figure 7 for a vehicle with specific velocity of v* = 20,000 ft/sec assuming again a constant view factor and surface emissivity of 1.0 and .9 respectively.

For the particular set of conditions selected, it is seen from Figure 7 that the lift needs to be negative throughout the major portion of the flight. This is required to prevent re-exit of the vehicle due to its super-circular velocity at high altitude. Entry velocities of 40,000 ft/sec for a vehicle with L/D_{max} capability of -1 are shown to be possible for earth entry. A "nose over" condition, requiring large negative lift is indicated towards the end

	v^* FT/SEC	v_o FT/SEC	γ_o °
1	10, 000	26, 000	1°
2	20, 000	26, 000	5°
3	40, 000	26, 000	15°
4	80, 000	36, 000	90°

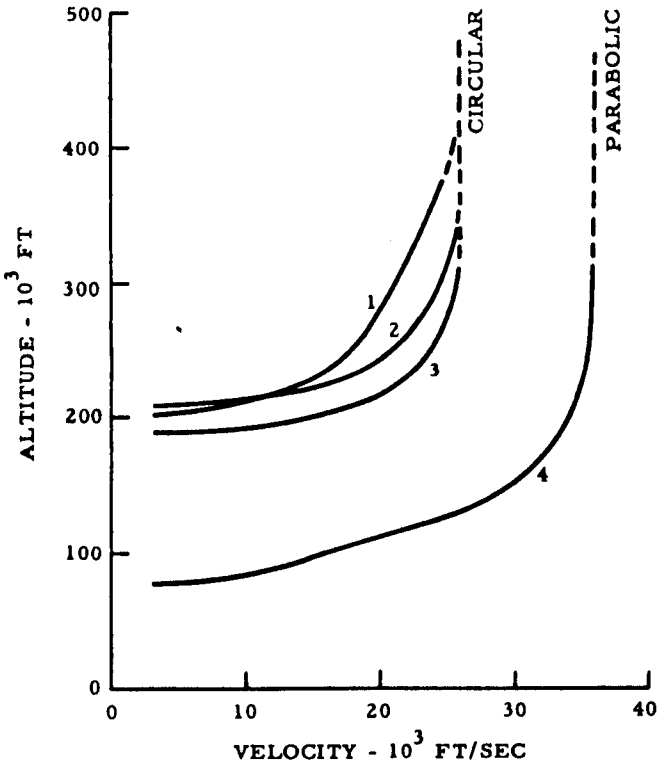

Figure 4. Drag Modulated Trajectories - Earth.

	v^* FT/SEC	v_o FT/SEC	γ_o
1	10, 000	11, 400	30°
2	20, 000	16, 900	30°
3	40, 000	16, 900	30°
4	80, 000	16, 900	90°

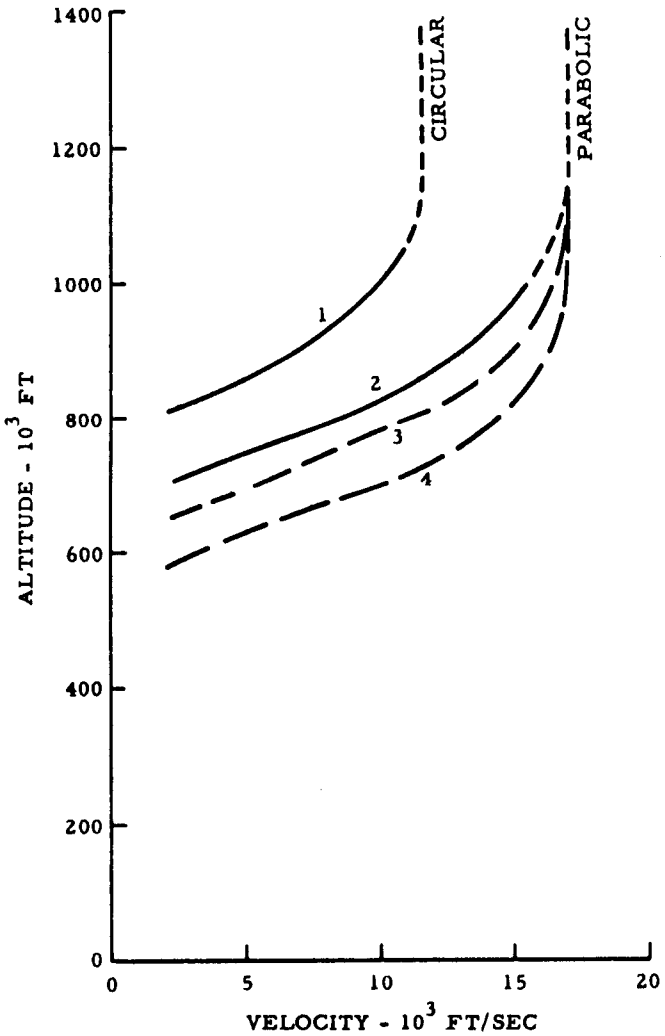

Figure 5. Drag Modulated Trajectories - Mars.

	v^* FT/SEC	v_o FT/SEC	γ_o °
1	10,000	23,300	6°
2	20,000	23,300	6°
3	40,000	23,300	20°
4	80,000	34,300	90°

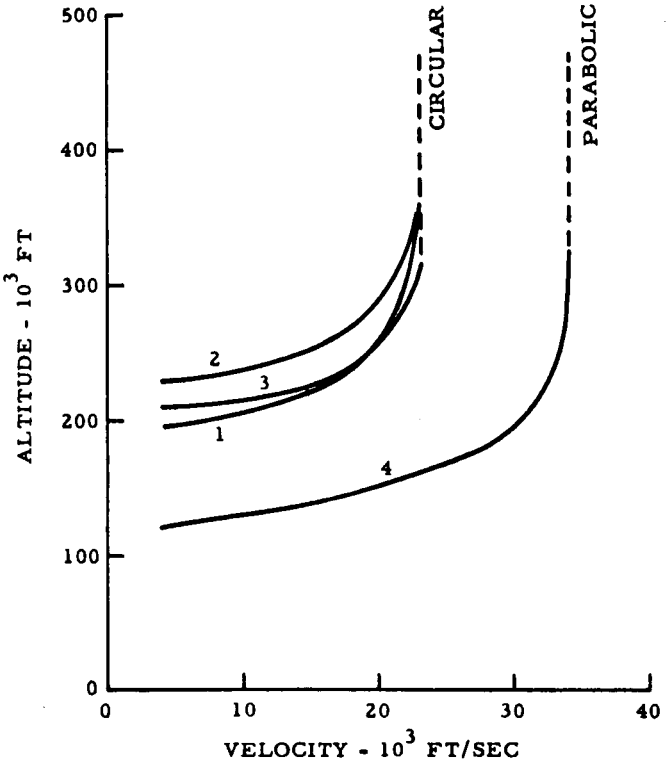

Figure 6. Drag Modulated Trajectories - Venus.

VEHICLE PARAMETERS

- $v^* = 20,000$ FT/SEC
- $\beta = 45°$
- $\frac{W}{A} = 0.2$ LB/FT^2
- $\theta = 780°$ C

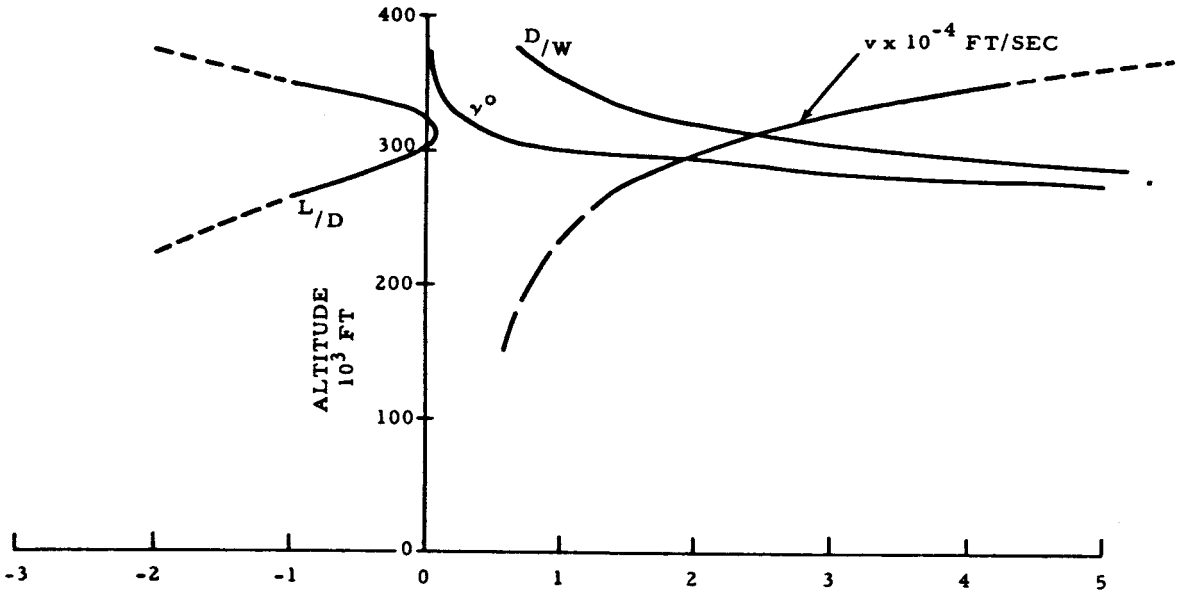

Figure 7. Typical Lift Modulated Trajectory - Earth.

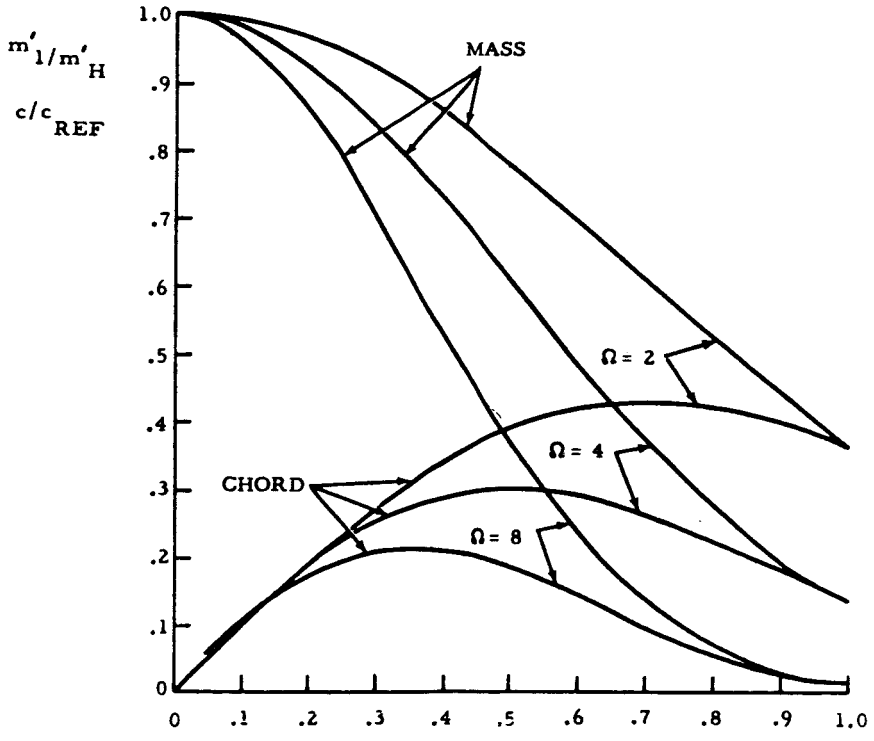

Figure 9. Chord and Mass Distribution for Ideal Rotor Blade.

of the isothermal flight phase. In practice, this maneuver would not be required, but rather a normal glide at reduced surface temperature would be followed.

C. Analytical Design of Bladed Rotors

For the purpose of a design evaluation, the bladed rotor configuration was selected for analysis.

For an optimum flexible rotor blade, two conditions need to be satisfied simultaneously:

- The spanwise distribution of cross-sectional area should be such, that the radial stress s is uniform throughout the structure (isotensoid condition). This allows to exploit completely the potential strength of the blade material.
- The slope of the spanwise blade axis (local coning angle β) should be such that the local heating rates are uniform.

The following assumptions will be made:

- The blades are sufficiently slender such that the blade stresses are parallel to the blade axis.
- The mass distribution of the rotor is proportional to the cross section required to carry the axial blade tension.
- Uniform heating rates are achieved by uniform blade slope, i. e., by a blade of zero meridional curvature.

Consider the forces acting on a blade element of unit differential spanwise length, cordwise width c and mass/unit length m', rotating with angular velocity ω as shown in Figure 8.

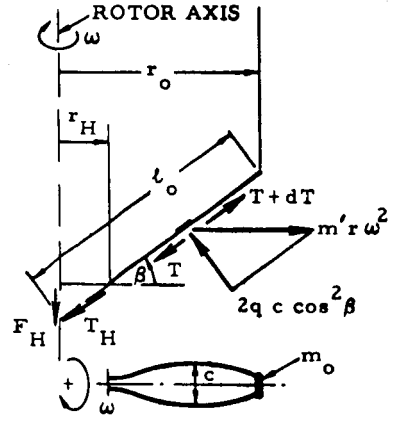

Figure 8. Rotor Blade Forces.

It is assumed that the aerodynamic pressure force arises from a complete transfer of the air momentum component perpendicular to the blade axis, resulting in a normal pressure of $2q\cos^2\beta$, where q is the free stream dynamic pressure. It is further assumed that blade mass inertia forces due to flight path accelerations are negligible compared to the centrifugal forces caused by rotation.

The equilibrium conditions tangential and normal to the blade axis then are:

$$-\frac{dT}{dr} = m' r \omega^2 \tag{5}$$

$$2qc\cos^2\beta = m' r \omega^2 \sin\beta \tag{6}$$

Eq. (5) can be integrated by considering

$$m' = \frac{dm}{d\ell} = \frac{dm}{dr}\cos\beta \text{ , and}$$

$$T = m' \frac{s}{\rho}$$

where ρ is the density and s is the stress in the blade material, yielding

$$m' = m'_H \, e^{-\frac{\Omega}{2}(R^2 - R_H^2)} \tag{7}$$

where m'_H indicates the mass/unit length at the hub radius r_H.

$$R = r/r_o \text{ and } R_H = r_H/r_o$$

are non-dimensional coordinates, and

$$\Omega = r_o^2 \omega^2 \frac{\rho}{s}$$

is a non-dimensional rotational frequency characteristic for the blade design.

The mass distribution given by eq. (7) (and, therefore, the rotor's cross-sectional area) does not vanish at the tip R = 1. Therefore, a concentrated tip mass, m_o, is required to satisfy the condition of constant stress:

$$m_o = \frac{\ell_o}{\Omega} m'_H \, e^{-\frac{\Omega}{2}(1 - R_H^2)} \tag{8}$$

This will normally be a small fraction of the total rotor mass.

From eq. (6), a relation between the chord distribution and mass distribution is derived that satisfies the condition of uniform coning angle:

$$c = c_{REF} \, R \, e^{-\frac{\Omega}{2}(R^2 - R_H^2)} \tag{9}$$

where the reference chord width is defined by

$$c_{REF} = m'_H \ell_o \frac{\omega^2 \tan\beta}{2q} = \frac{A}{\ell_o} \Omega \left[1 - e^{-\frac{\Omega}{2}(1-R_H^2)} \right]^{-1}$$

Figure 9 shows non-dimensional plots of the mass and chord distribution of rotor blades satisfying the condition of uniform stress and coning angles for a number of selected values of the non-dimensional rotational speed Ω .

The distributed rotor mass is obtained by integrating eq. (7). The result can be expressed in terms of the tabulated probability function

$$I_{p(x_1)} = \frac{2}{\sqrt{\pi}} \int_0^{x_1} e^{-x^2} dx$$

as

$$m_R = m_o + m'_H \ell_o \sqrt{\frac{1}{\Omega}} \; J_{(R_H, \Omega)} \qquad (10)$$

where

$$J_{(R_H, \Omega)} = \sqrt{\frac{\pi}{2}} \; e^{\frac{\Omega}{2} R_H} \left[I_{p(\sqrt{\Omega/2})} - I_{p(\sqrt{\Omega/2}\, R_H)} \right]$$

For practical values of Ω and R_H , the expression $J_{(R_H, \Omega)}$ will approximately equal $\sqrt{\pi/2}$.

The resultant force F_H , parallel to the rotor axis which is imparted to the payload mp is equal to the required trajectory deceleration, given in terms of Earth gravity $g\dot{\delta}$

$$F_H = T_H \sin\beta = m'_H \frac{s}{\rho} \sin\beta = m_P (n g\dot{\delta})$$

This permits computation of the relative mass fraction between the mass m_R of an ideal rotor and the payload mass m_P :

$$\frac{m_R}{m_P} = n \frac{\ell_o (SF)}{\lambda_{sp}} \frac{1}{\sin\beta} \sqrt{\frac{1}{\Omega}} \frac{J_{(R_H, \Omega)}}{1 - m_o / M_R} \qquad (11)$$

where λ_{sp} is the specific strength of the rotor material, and (SF) is the ratio of ultimate tensile strength to working stress (Safety Factor) employed in the rotor design. Note that the rotor mass fraction is a linear function of absolute size ℓ_o . This is an expression of the "square-cube law" well known in aircraft design.

With some transformation, eq. (11) can be written as

$$\frac{m_R}{m_P} = n \sqrt{\frac{g\dot{\delta} (SF)}{\omega^2 \lambda_{sp}}} \frac{1}{\sin\beta \cos\beta} \frac{J_{(R_H, \Omega)}}{1 - m_o / M_R} \qquad (12)$$

Here, the rotor mass fraction is seen to be inversely proportional to the rotational frequency. Since rotor stress is a direct function of tip speed, again, the rotor efficiency is penalized by size.

Introducing reasonable values for a series of rotors with a payload capability of 3000 lbs, the rotor structural mass fraction is found to range around 1% to 5%. For instance, let the designing condition of an entry condition be

$$n = 10$$

$$\beta = 45^\circ$$

Assume the rotor to be designed to rotate at $\omega = 10$ rad/sec, to be made from a material with a specific strength of $.5 \times 10^6$ in, and to be designed with a safety factor of 2 . For these values, the ideal structural rotor weight fraction becomes approximately 2%.

In many instances, the weight of the rotor will not be determined by strength considerations, but by considerations of minimum practical material thickness at the rotor tips. In this case, the "constant stress" rotor mass is determined by

$$m_R = A \rho t_{min} \sqrt{\Omega} \; J_{(R_H, \Omega)} + m_o \qquad (11)$$

The rotor mass given by eq. (11) does not necessarily represent a minimum, since gage considerations may only affect a portion of the blade area, allowing the stress to be higher at the root than at the tip.

Another consideration is that of distributed rotor masses associated with surface area covering in addition to that required by structural strength alone. Such non-structural "parasitic" masses affect both the structural mass distribution and the chord distribution of an ideal blade. Analytical design equations similar to those presented in this paragraph have been developed for this case. Their detailed presentation is omitted from this paper for the sake of brevity.

D. Materials Selection for High Temperature Rotors

The material to be used in the construction of rotors needs to be formed into thin, flexible membranes or fabrics. Fortunately, an extensive effort has been directed, during the past few years, towards the study and development of temperature resistant, packageable filament and fabric-type materials, particularly for application of high speed parachutes, temperature resistant filament wound structures and others (Ref. 9-11).

In comparing the relative merits of candidate materials, a controlling parameter is their ability to maintain a useful tensile strength for a given structural mass while rejecting thermal energy by radiation. This leads to the definition of a materials parameter

$$Q = \sigma \epsilon \theta^4 \lambda_{sp}$$

Since both, the emissivity ϵ and the specific strength are temperature dependent, Q , will be an empirical function of temperature, normally rising to a maximum value after which the degradation of strength becomes stronger than the increase in radiative power dissipation.

In practice, the situation is further complicated by the fact that the strength is not only a function of temperature but also of the previous load-temperature history. For the purpose of this discussion it was decided to compare materials on the basis of their short term strength-at-temperature characteristics which may be considered reasonably representative for the intended operation of the rotor configuration during atmospheric entry.

Values for strength and surface emissivity for candidate materials were collected from numerous reference sources. These data were reduced to Q-values and represented on the composite graph of Figure 10. The outstanding potential of elemental boron fibers in the particularly interesting temperature range from 400° C to 1200° C is readily apparent from this graph.

Since little reliable data on this relatively new material were available, a laboratory setup for the production of experimental quantities of continuous boron filaments was constructed. Filaments of approximately 2 mil diameter were produced and subject to tensile tests at temperatures up to 1200° C in inert atmosphere and air. In addition, several composites and laminates were made with elemental boron fiber base materials. The test data, as reflected in Figure 10, generally confirm the exceptional physical properties of this material.

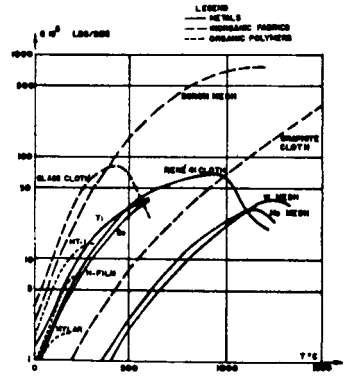

Figure 10. Material Parameter Q vs. Temperature.

For rotors that can operate at very low v* -values (for shallow entry) equilibrium temperatures of 400° C and less appear to be practical. For this application, various types of glass or temperature resistant synthetic textile fabrics can be considered.

Alternatively for small, highly loaded rotors, such as may be required for "straight in" trajectories, v* -values of the order of 80,000 ft/sec may be required. For these missions, carbon or graphite cloth may be considered for planetary entry into non-oxidizing atmospheres.

E. Experiments

A number of rotor models have been fabricated and subject to qualitative tests in a low speed vertical tunnel. The models were designed to represent the three basic configurational control schemes—bladed rotor, fluted cone and spiral net—discussed previously. The tests were conducted to observe the ability of the various model to deploy themselves in an axial airstream, and to autorotate at various coning angles and through a range of angles of flow incidence.

The airstream velocity in the test section of the tunnel was 14 ft/sec generating a dynamic pressure of approximately .22 psf. The configuration of the model rotors are such that in most cases stalled or near-stalled flow conditions prevailed, thus the aerodynamic characteristics of hypersonic flow are approached at least qualitatively.

Characteristic flutter motions in non mass balanced blades and deployment dynamics of the various rotors were observed and recorded by motion picture. Rotational speeds were measured by means of strobelight, airspeed by means of a torque vane. No attempt was made to obtain quantitative lift and drag data. It was observed, however, that most rotors would more than support their own weight in axial flow, indicative of normal force coefficients based upon disk area in excess of 1 to 1.5.

Bladed Rotors

Figure 11 shows a typical bladed rotor made from thin mylar film, rotating with essentially zero coning angle at approximately 220 rpm and an angle of flow incidence of approximately 70° . It

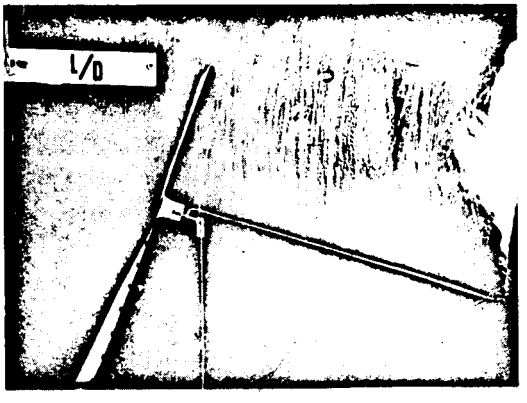

Figure 11. Mylar Film Blade in Autorotation at Incidence Angle of 70° .

was found that the blade center of gravity axis needs to be placed slightly forward of the 25% chord line to prevent torsion-bending blade flutter. Balancing is accomplished by small lead weights clamped to the leading edges of each blade. The rotor is completely flexible, mounted to a bearing supported hub that can be tilted during operation through a 90° angle, simulating flight at various angles of incidence. This model deployed automatically if subject to an axial airstream and maintained stable autorotation throughout a 70° range of inflow incidence.

Fluted Cone

Figure 12 shows a model of a fluted cone configuration, made from dacron fabric. Tip weights are attached to short chain links at each seam of the convoluted configuration. The convolutions are tailored to form a spiral groove causing the configuration to be driven into rotation by the axial airstream. Automatic deployment at low axial flow velocities was achieved. Significant angles of flow incidence could not be maintained with this model.

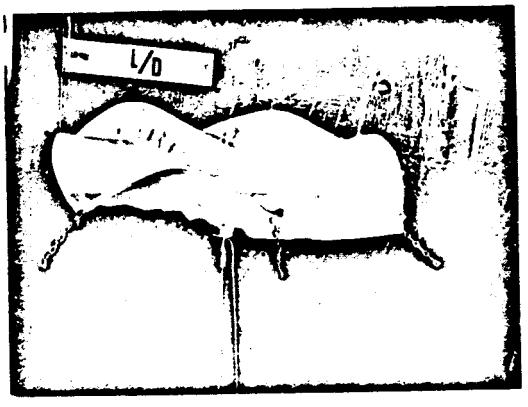

Figure 12. Fluted Cone in Axial Flow.

Spiral Net

An open mesh spiral net model in axial flow is shown in Figure 13. Autorotation is maintained by impeller tabs fastened to the periphery of the net. Tilting of the hub axis, as shown, did not affect the rotors tendency to be oriented with its plane normal to the airstream. The same net is shown with an aerodynamic covering in Figure 14. Both configurations deployed automatically in axial stream and maintained stable rotation through a range of coning angles.

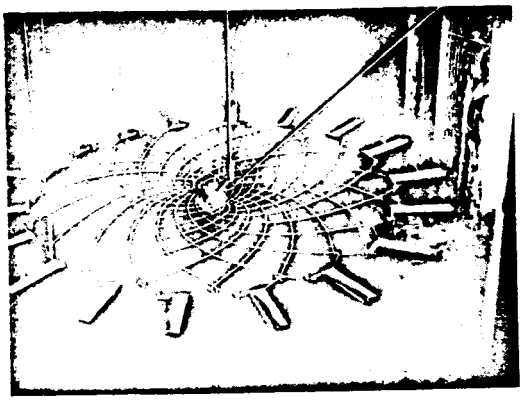

Figure 13. Spiral Net Rotor with Tip Impeller Tab.

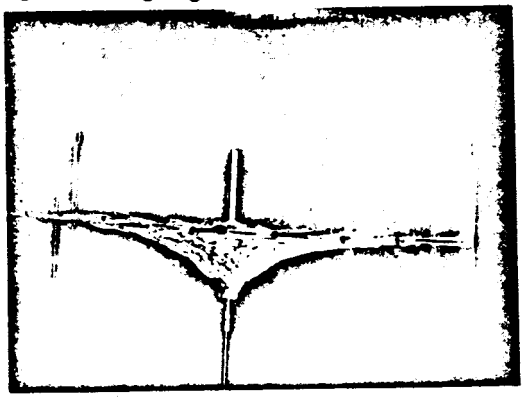

Figure 14. Spiral Net Rotor with Aerodynamic Cover.

A composite configuration of two nets mounted with hubs spaced by a shaft is shown in Figure 15. The upper net is open, as shown in Figure 15, the lower net is covered to provide aerodynamic surface. Coning angle control of this configuration is affected by varying the distance of the two hubs on the shaft. This configuration proved capable of maintaining stable rotation at incidence angles up to approximately 45°.

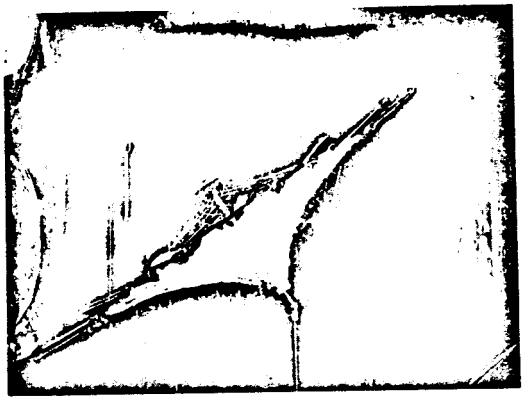

Figure 15. Composite Spiral Net Rotor.

F. Application

A number of mission profiles as reflected by the trajectory requirements have been studied in view of the particular design configurations required. A conceptual design for a vehicle, capable of Mars entry with an initial flight path angle of 30° from parabolic velocity and return into earth atmosphere with an initial path angle of 5° from

circular orbit is shown in Figures 16, 17, and 18. Figure 16 shows a deployed "low q" configuration of the vehicle required for the initial entry and terminal flight phase.

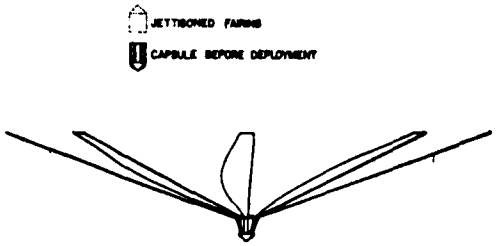

Figure 16. Deployed Rotor - Low q Configuration.

Figure 17 shows the required "high q" configuration at maximum deceleration with a coning angle of 70°.

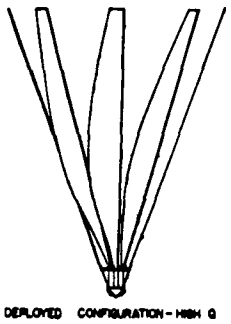

Figure 17. Deployed Rotor - High q Configuration.

Some details of the capsule arrangement with the packaged rotor are shown in Figure 18.

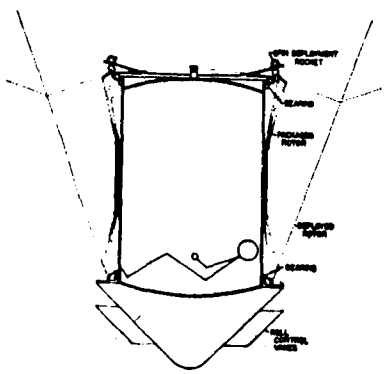

Figure 18. Packaged Rotor and Capsule Concept.

The design characteristics selected for this vehicle are:

Total mass	:	2000 lbs
Rotor area	:	10,000 ft^2
v*	:	20,000 ft/sec
Q	:	$.33 \times 10^9$ lbs/sec
Maximum deceleration:		10 g_o^+

Rotor design data are as follows:

Blade parameter Ω	:	4
Blade length ℓ_o	:	135 ft
Temperature	:	760° C
Design safety factor	:	2
Structural weight of ideal rotor	:	43.7 lbs
Tip weights (total of 8)	:	2.4 lbs

The structural requirements for the particular configuration selected leads to extremely low blade thickness (1.3 mil at the root). Thus, it would be expected that a "practical" design will employ a heavier rotor by perhaps a factor of 5. Even if this penalty is accepted, the payload mass fraction would appear to compare favorably with ablation-protected entry capsules. It points, however, to the desirability of developing extremely thin, heat resistant fabric and film materials for this application.

References for Part I

1 Koelle, H. (editor): "Handbook of Astronautical Engineering," McGraw-Hill, New York, 1961.

2 Slivka, L. P.: "Development of Pneumatic Structural Material for Helicopter Rotor Blades," Goodyear Aircraft Corp. Report No. GER-7236, Jan. 1956.

3 Wornom, D. E., Taylor, R. T.: "Aerodynamic Characteristics of a Flexible-Canopy Paraglider Model at a Mach Number of 4.5 for Angles of Attack to 360° and Sideslip Angles from 0° to 90°," NASA TN D-1776, April 1963.

4 Alexander, W. C.: "Investigation to Determine the Feasibility of Using Inflatable Balloon Type Drag Devices for Recovery Applications in the Transonic, Supersonic, and Hypersonic Flight Regime - Part II: Mach 4 to Mach 10 Feasibility Investigation," Goodyear Aircraft Corp., ASD-TDR-62-702, Pt. II, December 1962.

[5] Packard, C. B.: "Final Report of KRC-4 Rotochute Development," Kaman Aircraft Corporation, Report No. R-239, August 1958.

[6] Schuerch, H.: Contract NASw-652, Final Report (In Preparation)

[7] Burggraf, O., Schuerch, H.: "Analysis of Axisymmetric, Rotating Pressurized Filamentary Structures," Astro Research Corporation, NASA TN D-1920, May 1963.

[8] Schuerch, H., Schindler, G.: A Contribution to the Theory of Folding Deformations in Expandable Structures with a Particular Application to Toroidal Shells," Astro Research Corporation, NASA TN D-1690, December 1962.

[9] Ross, J. H.: "Symposium on Fibrous Materials," Aeronautical Systems Div., ASD-TDR 62-964, January 1963.

[10] Coplan, M. J. et al: "Flexible, Low Porosity, Woven Metallic Materials," Fabric Research Laboratories, Inc., ASD TR 61-677, November 1961.

[11] Kolarik, R. V., Marco, D. M.: "New and Improved Materials for Expandable Structures - Phase IV - High Temperature Protective Study," Goodyear Aircraft Corporation, ASD-TDR-62-542, Part V, February 1963.

[12] National Aeronautics & Space Adm: "U. S. Standard Atmosphere - 1962."

PART II

HYPERSONIC ROTOR DYNAMICS

Introduction

The desirability of very low density centrifugally stabilized drag and lift producing autorotating surfaces has been discussed in Part I of this paper. A critical problem area is that of flight dynamics of rotary wing vehicles in hypersonic flow. Since opportunities for testing free flight models under hypersonic conditions will be rare, analytical procedures must be used to the fullest extent to determine the stability and control characteristics of rotary wing re-entry devices.

Little precedent exists for this type of analysis. The analysis presented in this preliminary study, therefore, is developed from basic concepts of Newtonian flow and with a minimum of originally restrictive assumptions. The presentation given here confines itself to the development of the pertinent equations, suitable for processing on digital computers. It is intended to apply this method to one or several typical rotor configurations to obtain insight into the feasibility of proposed design concepts.

A. Aerodynamic Forces

In an autorotative descent with very large thru-flow velocity, rotor speed stability requires that the angle of attack of the blades be near either zero degrees or near ninety degrees. The large angle of attack (corresponding to the wind-mill braking state) is selected for hypersonic re-entry because it results in much larger rotor thrust. Expressions for aerodynamic forces on rotor blades at large angles of attack are developed in Reference 1 for Mach numbers from 0.5 to 3.0, and are applied to the performance characteristics of a rotating decelerator. For Mach numbers above 3.0 and angles of attack greater than 10°, simple Newtonian flow theory is adequate for the evaluation of rotor dynamic response, and the estimation of performance.

In this section of the report a general theory of hypersonic rotor dynamic response will be developed by the blade element approach using Newtonian aerodynamics. The results will be applied to the determination of trim conditions for lifting flight (non-zero L/D) and to the calculation of vehicle dynamic stability. Unexplored problem areas to which the theory can also be applied include vibrations, flutter and dynamic loads.

It will be assumed that a rotor "blade" is a thin sheet, that the tangential aerodynamic force on the sheet can be neglected (except in rotor speed calculations), and that the aerodynamic force normal to the blade on the side opposite to the flow is zero. Then, according to Newtonian flow theory, the aerodynamic force normal to an element, S, of blade area is

$$F_n = \rho S v_n |v_n| \qquad (A\text{-}1)$$

where ρ is the density of the air and v_n is the component of the velocity of the undisturbed flow normal to the element of area. The absolute value sign is used to indicate that the force changes sign when the flow impinges on the reverse side of the element. In order to avoid mathematical difficulties it will be assumed that, under all conditions, $v_n > 0$; in other words, that the flow always impinges the lower side of the blade element. This assumption must be remembered in applying the results to extreme cases.

The first task in developing the theory is to calculate the aerodynamic force on a blade element in response to the motions of the blade element and the translational velocity of the rotor. The components of motion and the coordinate systems to be used in the analysis are shown in Figure 1. The x, y, z coordinate system rotates with constant angular velocity ω about the z-axis. The axes x_s y_s and z are inertial axes that translate with velocity components U and V with respect to the atmosphere. The axis of one blade is assumed to be in (or near) the y-z plane except for dynamic motions and small static offsets. The velocity components of a blade element, in the x, y, z coordinate system relative to the airstream are

$$\begin{aligned} v_x &= \dot{x} - \omega y - V \sin \psi \\ v_y &= \dot{y} + \omega x - V \cos \psi \\ v_z &= \dot{z} - U \end{aligned} \qquad (A\text{-}2)$$

Consider a blade element whose normal is tilted with respect to the coordinate system as shown in Figure 2. β is the coning angle and θ is the pitch angle about the blade axis. The component of velocity normal to the blade element is

$$v_n = -v_x \sin\theta + v_y \cos\theta \sin\beta - v_z \cos\theta \cos\beta \qquad (A\text{-}3$$

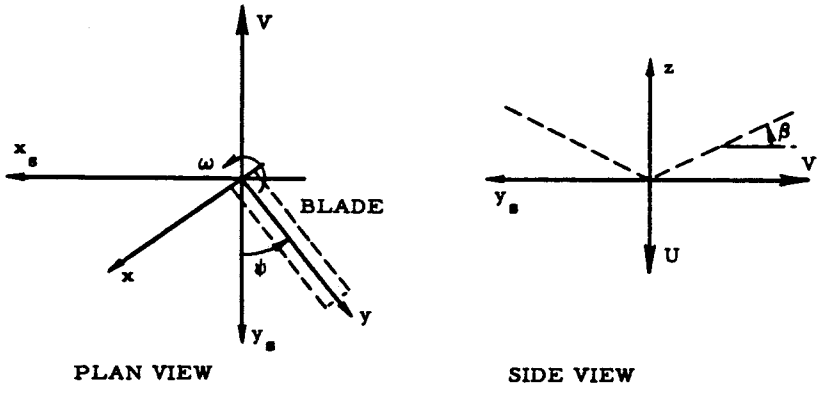

Figure 1. Coordinate Systems.

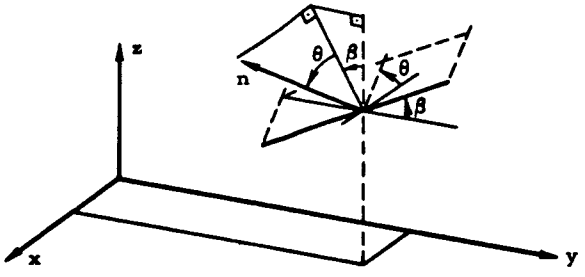

Figure 2. Direction of Normal to Blade Element.

Substituting into eq. (A-1) and assuming that $v_n > 0$ the force on the blade element is

$$F_n = \rho S \Big\{ (-\dot{x} + \omega y + V \sin\psi)^2 \sin^2\theta + (\dot{y} + \omega x - V\cos\psi)^2 \cos^2\theta \sin^2\beta + (-\dot{z} + U)^2 \cos^2\theta \cos^2\beta + 2(-\dot{x} + \omega y + V\sin\psi)(\dot{y} + \omega x - V\cos\psi)\sin\theta\cos\theta\sin\beta + 2(-\dot{x} + \omega y + V\sin\psi)(-\dot{z} + U)\sin\theta\cos\theta\cos\beta + 2(\dot{y} + \omega x - V\cos\psi)(-\dot{z} + U)\cos^2\theta\sin\beta\cos\beta \Big\} \quad (A\text{-}4)$$

The complete generality afforded by this equation will not often be required. For many applications it is satisfactory to assume that $x = 0$, that θ is small, and that $\dot{x}$ and $\dot{y}$ are small compared to the other components of velocity. In this case eq. (A-4) reduces to

$$F_n = \rho S \Big\{ (U\cos\beta - V\cos\psi\sin\beta)^2 - 2\dot{y}(V\cos\psi\sin^2\beta - U\sin\beta\cos\beta) - 2\dot{z}(U\cos^2\beta - V\cos\psi\sin\beta\cos\beta) + 2\theta(\omega y + V\sin\psi)(U\cos\beta - V\cos\psi\sin\beta) \Big\} \quad (A\text{-}5)$$

This expression is adequate for treating small perturbations of rotor motion at small pitch angles but with arbitrarily large coning angles and arbitrary angles of incidence of the flight path with respect to the rotor plane, provided only that $\tan\beta < U/V$, in order to avoid flow impingement on the top surface.

Resultant forces and moments are obtained by multiplying F_n by appropriate geometrical factors and integrating over the surface of the rotor blades.

B. Rotor Trim Conditions for Lifting Flight

The rotors considered in this report are characterized by extremely flexible blades that have virtually no bending stiffness in the flapwise direction. In steady flight the thrust of such a rotor must be very nearly perpendicular to the tip-path plane, as shown in Figure 3, because the oscillating component of blade tension is necesarily small compared to the steady centrifugal tension.

The ratio of lift to drag for the rotor is simply

$$L/D = \tan\alpha = V/U \quad (B\text{-}1)$$

An additional result of extreme blade flexibility and small flapping hinge offset is that the moment, M, exerted by the rotor on the hub is very small. In order to obtain a positive criterion for trimmed flight, we shall assume that the steady aerodynamic moment on the hub is zero.

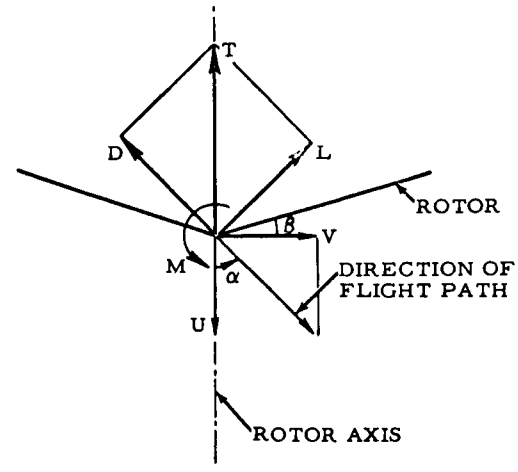

Figure 3. Rotor in Steady Lifting Flight.

In the absence of the cyclic variation of some rotor parameter, the aerodynamic force will be greater on a blade when it is in the forward position ($\psi = \pi$) than when it is in the trailing position, due to the finite coning angle, β. Cyclic pitch is the conventional means for controlling the angle of incidence of a subsonic helicopter and it can also be employed in hypersonic flight. From eq. (A-3), the component of velocity normal to an element of blade area is, in the absence of dynamic motions:

$$v_n = (\omega y + V\sin\psi)\sin\theta - V\cos\psi\cos\theta\sin\beta + U\cos\beta\cos\theta \quad (B\text{-}2)$$

Let $\theta = \theta_1 \cos\psi$ and calculate the normal component of velocity for $\psi = 0, \pi/2, \pi$ and $3\pi/2$

$$v_n(0) = \omega y\sin\theta_1 - V\cos\theta_1\sin\beta + U\cos\theta_1\cos\beta$$

$$v_n(\pi/2) = v_{n(3\pi/2)} = U\cos\beta$$

$$v_n(\pi) = -\omega y\sin\theta_1 + V\cos\theta_1\sin\beta + U\cos\theta_1\cos\beta$$

An approximate condition for trim is obtained by equating the moments in the zero and 180° azimuth positions:

$$\int \rho y\, v_n^2(\pi)\cos^2\theta_1\, dS = \int \rho y\, v_n^2(0)\cos^2\theta_1\, dS$$

which results in the required cyclic pitch

$$\tan\theta_1 = \frac{V}{\omega\bar{y}}\sin\beta \quad (B\text{-}3)$$

where

$$\bar{y} = \int y^2\, dS / \int y\, dS$$

and it is assumed that β is constant along the span of the blade.

The effective "advance ratio" for the rotor,

$V/\omega\bar{y}$ may be very large (of the order of 10) in hypersonic re-entry. Furthermore, β will not be small if the rotor weight is small compared to the thrust so that the required cyclic pitch angle may be quite large. This result discourages the use of cyclic pitch to obtain lift, particularly since the collective pitch required for practical rotor speeds is very small.

An alternative to cyclic blade pitch is the use of flaps to produce an effective cyclic variation in blade area by the mechanism shown in Figure 4 or in some other way.

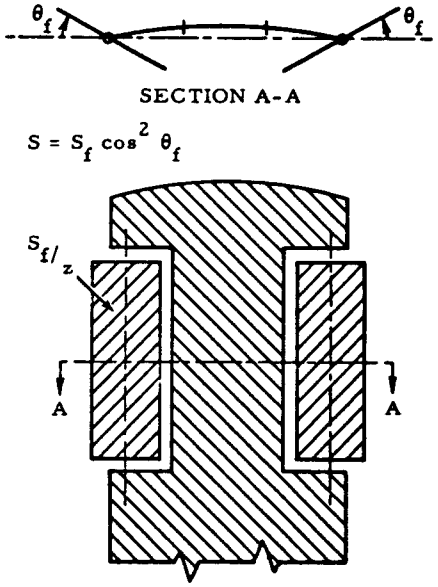

Figure 4. Flaps for Producing Effective Change in Blade Area.

Let the effective area of a blade element be

$$S = S_0 + S_1 \cos\psi \qquad \text{(B-4)}$$

and calculate the first harmonic (one/rev) component of aerodynamic force on the blade element from the first term in eq. (A-5). (First harmonic force in the rotating coordinate system results in steady moment in the non-rotating system). The result is

$$F_{n_1} = \rho \cos\psi \left[-2 S_0 \, U V \sin\beta \cos\beta + S_1 \left(\frac{3}{4} V^2 \sin^2\beta + U^2 \cos^2\beta \right) \right] \qquad \text{(B-5)}$$

For a blade in which the ratio S_1/S_0 is uniform along the span, zero first harmonic flapping moment is achieved if

$$S_1/S_0 = \frac{2 U V \sin\beta \cos\beta}{\frac{3}{4} V^2 \sin^2\beta + U^2 \cos^2\beta} \qquad \text{(B-6)}$$

which for small β reduces to

$$S_1/S_0 = 2 V/U \tan\beta = 2 L/D \tan\beta \qquad \text{(B-7)}$$

Thus for small coning angles and reasonable values of L/D the required percentage variation in area may not be unreasonably large.

Because coning angle is the reason for the aerodynamic overturning moment in lifting flight, we are led to a consideration of means for eliminating the effective aerodynamic coning of the rotor. This is accomplished by the tip flapping vanes shown in Figure 5. This configuration is aerodynamically a hybrid of a conventional rotor (concave upward) and a parachute (concave downward).

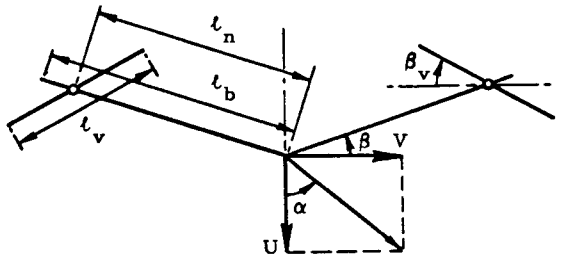

Figure 5. Rotor with Tip Vanes.

The general idea is that the reverse coning, β_v, of the vanes decreases the aerodynamic force on the forward blade and increases it on the aft blade. The aerodynamic force on a blade element per unit of span is

$$F_{n_b} = \rho c \left\{ U \cos\beta - V \sin\beta \cos\psi \right\}^2 \qquad \text{(B-8)}$$

while for the vane

$$F_{n_v} = \rho c_v \left\{ U \cos\beta_v + V \sin\beta_v \cos\psi \right\}^2 \qquad \text{(B-9)}$$

If the chords c and c_v are uniform along the span then the moment about the hub is

$$M = \frac{\ell_b^2}{2} F_{nb} + \ell_v \ell_n \cos(\beta_v + \beta) F_{nv} \qquad \text{(B-10)}$$

and substituting for F_{nb} and F_{nv}

$$M = \frac{\rho c \ell_b^2}{2} \left\{ U^2 \left[\cos^2\beta + K_v \cos^2\beta_v \cos(\beta_v + \beta) \right] - 2UV\cos\psi \left[\sin\beta\cos\beta - K_v \sin\beta_v \cos\beta_v \cos(\beta_v + \beta) \right] + V^2 \cos^2\psi \left[\sin^2\beta + K_v \sin^2\beta_v \cos(\beta_v + \beta) \right] \right\} \qquad \text{(B-11)}$$

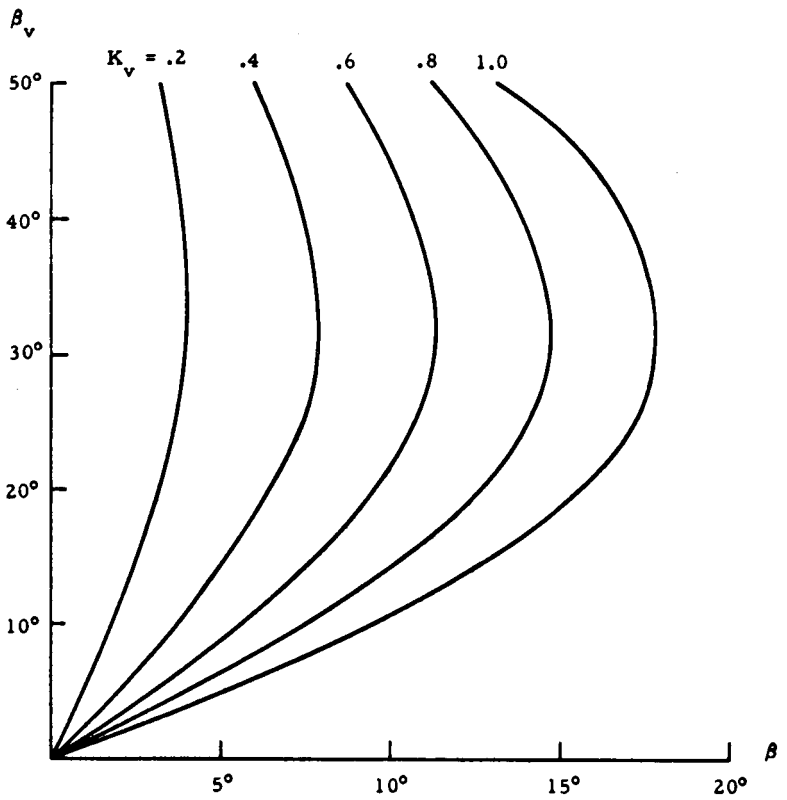

Figure 6. Vane Reverse Coning for Trimmed Lifting Flight.
(See Eq. B-13)

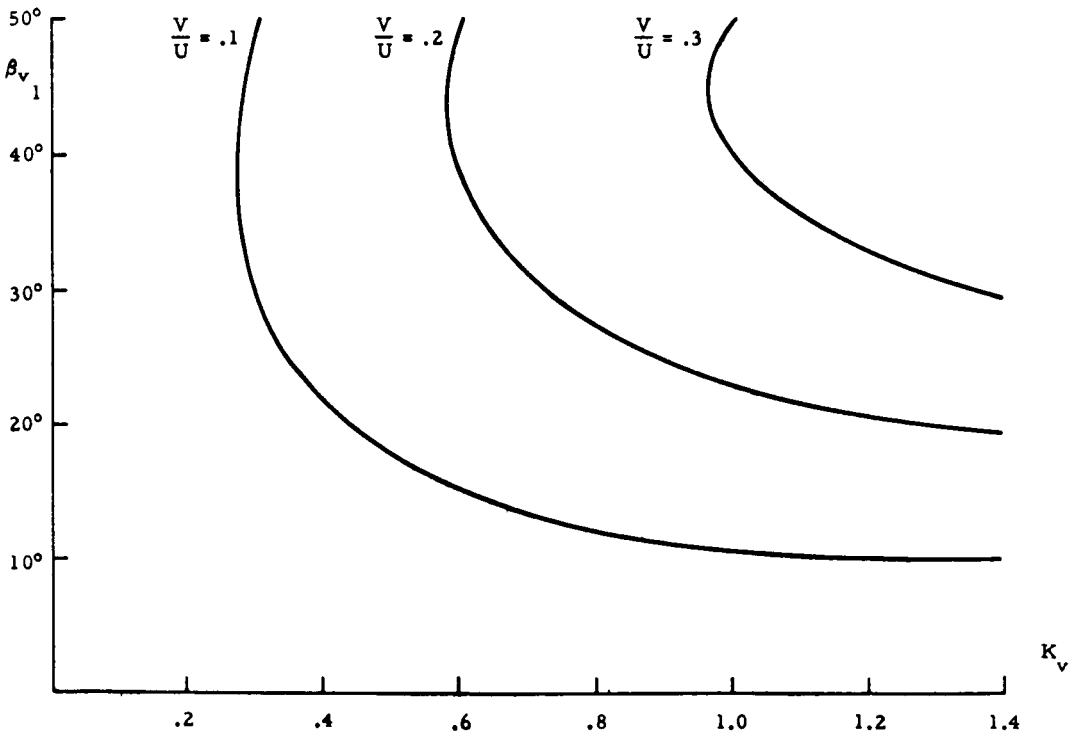

Figure 7. Vane Cyclic Coning for Trimmed Lifting Flight.
(See Eq. B-15)

where

$$K_v = \frac{2\ell_v \ell_n c_v}{\ell_b^2 c} \qquad \text{(B-12)}$$

To achieve zero one/rev component of moment the coefficient of $\cos\psi$ should be zero. Therefore, to achieve this condition with constant β_v

$$\sin\beta \cos\beta = K_v \sin\beta_v \cos\beta_v \cos(\beta_v + \beta) \qquad \text{(B-13)}$$

The relationship between β_v and β for different values of K_v are plotted in Figure 6. It will be noted that for a given K_v there is a maximum value of β for which trim can be achieved and that, for practical values of K_v, the maximum value of β is 20° or less.

An interesting fact is that the condition of trim is independent of $\alpha = \tan^{-1} L/D$ (except indirectly since β depends to some extent on α). Thus, the effect of a vane angle set to satisfy eq. (B-13) is to eliminate the static stability of the rotor with regard to overturning moment. A reduction rather than complete elimination of static stability may be desirable so that we are led to a consideration of a combination of a constant vane angle somewhat less than that given by (B-13) plus a cyclic variation of β_v

$$\beta_v = \beta_{v_0} + \beta_{v_1} \cos\psi \qquad \text{(B-14)}$$

For $\beta_{v_0} = -\beta$, the vane flaps cyclicly with respect to the cone generated by the rotor blade thus representing a condition of pure cyclic control, and for this case the condition of zero overturning moment is:

$$(V/U)^2 \sin^2\beta_{v_1} + V/U\left(\frac{1}{K_v} + \cos\beta_{v_1} \cos 2\beta_{v_1}\right)$$

$$- \sin\beta_{v_1} \cos^2\beta_{v_1} = 0 \qquad \text{(B-15)}$$

Note that this result is independent of β.

V/U is plotted in Figure 7 for several values of K_v. For reasonable values of K_v, the obtainable value of V/U is fairly small.

Consider, finally, a case where most of the aerodynamic trim is provided by β_{v_0} so that β_{v_1} may be assumed to be small. Under these conditions

$$\frac{1}{K_v} V/U \left(\sin 2\beta - K_v \cos(\beta + \beta_{v_0}) \sin 2\beta_{v_0}\right) =$$

$$= \beta_{v_1} \left\{\sin^2\beta_{v_0} \sin(\beta + \beta_{v_0}) - \sin(\beta + 3\beta_{v_0}) + \right. \qquad \text{(B-16)}$$

$$\left. + (V/U)^2 \left[\sin(\beta + 3\beta_{v_0}) + \cos^2\beta_{v_0} \sin(\beta + \beta_{v_0})\right]\right\}$$

The left side of this equation represents the portion of the overturning moment that is not trimmed by collective vane angle. The coefficient of β_{v_1} changes sign for a value of V/U that is approximately equal to

$$\sqrt{\frac{\beta + 3\beta_{v_0}}{2\beta + 4\beta_{v_0}}}$$

Near this value eq. (B-16) is not valid since it results in a large value of β_{v_1}. Below this value the rotor is statically stable with regard to overturning moment if the left hand side of the equation is positive. No conclusion regarding overall vehicle stability can justifiably be drawn from this statement at the present time because the connection between rotor static stability and vehicle dynamic stability has not been explored.

C. Dynamic Equations of Blade Motion

Equations of rotor motion will be developed that are suitable for the analysis of the complete vehicle for small lateral perturbations from axial flight. It will be assumed that each rotor blade has a single degree of freedom, β_1, consisting of a rigid rotation about an offset flapping hinge. In addition, the hub has four degrees of freedom, consisting of two lateral translations and two rotations about lateral axes. In an analysis of the complete vehicle the rotor will be represented by relationships between motions of the hub and the resulting forces and moments on the hub. In this section equations will be written for a single blade in terms of its flapping degree of freedom and the four degrees of hub motion x_n, ϕ_n, y_n, θ_n. The degrees of freedom and basic dimensions are shown in Figure 8.

The flapping angle consists of a constant part β_c and a small dynamic perturbation β_1. The coordinate system rotates with angular velocity ω about the z-axis.

An important simplification in analysis and in the presentation of results occurs if the steady inertia and aerodynamic forces are distributed along the blade in such a way that the equilibrium shape of the blade is a straight line. This condition is satisfied if

$$\rho c U^2 \cos^2\beta_c = m' r \omega^2 \sin\beta_c \qquad \text{(C-1)}$$

where c is the chord of the blade, m' is the mass per unit length and r is the distance from the axis of rotation. With this assumption, the mass density of a uniform chord blade is proportioned to $1/r$. It is further assumed that there is no mass inboard of the flapping hinge.

Under the assumptions stated above the homogeneous equation of blade flapping in the absence of hub motions is

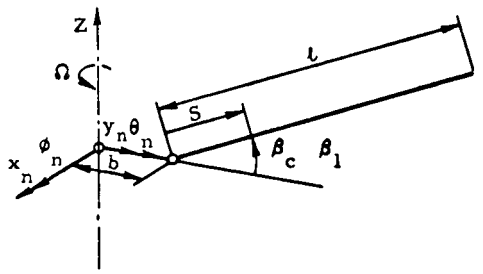

Figure 8. Degrees of Freedom for Rotor Blade Analysis.

$$\ddot{\beta}_1 + 2\omega \rho_b \beta_1 + \omega^2 + \omega_b^2 = 0 \qquad \text{(C-2)}$$

where

$$\omega_b^2 = \omega^2 \frac{b\ell_{01}}{\ell_{02}^2} (\cos\beta_c + 2 \sin\beta_c \tan\beta_c)$$

$$\zeta_b = \omega/U \frac{\ell_{12}^3}{\ell_{02}^2} \tan\beta_c$$

$$\ell_{01} = \frac{1}{m_b} \int_0^\ell m' s ds ; \ell_{02}^2 = \frac{1}{m_b} \int_0^\ell m' s^2 ds ;$$

$$\ell_{12}^3 = \frac{1}{m_b} \int_0^\ell m' r s^2 ds$$

$$m_b = \int_0^\ell m' ds$$

It will be observed that the effect of an offset flapping hinge is to raise the natural frequency of vibration above ω by an amount that increases with increasing β_c. The critical damping coefficient ζ_b is equal to the product of $\tan\beta_c$ and a number that is proportional to tip speed ratio. As an example, consider the following conditions that might exist at maximum dynamic pressure during re-entry.

$\omega\ell$ = 2000 ft/sec

U = 16000 ft/sec

β_c = 20°

Then, for a blade with uniform mass and zero flapping hinge offset

$$\zeta_b = \frac{\omega\ell}{U} \tan\beta_c \times \frac{3}{4} \cos\beta_c = .032$$

which is about one-tenth of the usual value for a subsonic rotor.

The general equations of motion including hub motions can be written in the following partitioned matrix form

$$\begin{Bmatrix} F_{x\,n} \\ F_{y\,n} \\ M_{\phi\,n} \\ M_{\theta\,n} \\ \hline M_{\beta_1} \end{Bmatrix} = \left[\begin{array}{c|c} & \\ H_n & H_\beta \\ & \\ \hline B_n & B_\beta \end{array}\right] \begin{Bmatrix} x_n \\ y_n \\ \phi_n \\ \theta_n \\ \hline \beta_1 \end{Bmatrix} \qquad \text{(C-3)}$$

The twenty-five coefficients in this equation are listed in Appendix I. These coefficients are derived from three sources—the stiffening effects of the static centrifugal forces and the static aerodynamic load, the perturbation inertia forces including Coriolis effects, and the perturbation aerodynamic forces. Eq. (A-4) was used as the basic source of aerodynamic coefficients and the constant coning angle assumption (eq. (C-1)), was employed.

The forces and moments on the hub can be expressed in terms of the motions of the hub by eliminating β_1 from eq. (C-3), with the result

$$\begin{Bmatrix} F_{x\,n} \\ F_{y\,n} \\ M_{\phi\,n} \\ M_{\theta\,n} \end{Bmatrix} = \left[H_n - H_\beta B_\beta^{-1} B_n \right] \begin{Bmatrix} x_n \\ y_n \\ \phi_n \\ \theta_n \end{Bmatrix} \qquad \text{(C-4)}$$

This expression can only be interpreted as a matrix of transfer functions in terms of the derivative operator, p , because of the presence of the inverse of B_β .

D. Lateral Rotor Derivatives

When analyzing the stability of the vehicle as a whole it is convenient to express the relationship between the forces and moments on the hub and the motions of the hub in terms of a matrix of frequency-dependent transfer functions. For small perturbations from axial flight, symmetry of the rotor permits the transfer functions for lateral motions to be written as follows in the non-rotating coordinate system:

$$\begin{Bmatrix} F_{x\,s} \\ F_{y\,s} \\ \hline M_{\phi\,s} \\ M_{\theta\,s} \end{Bmatrix} = \left[\begin{array}{cc|cc} X_x & -Y_x & X_\phi & -Y_\phi \\ Y_x & X_x & Y_\phi & X_\phi \\ \hline \Phi_x & -\theta_x & \Phi_\phi & -\theta_\phi \\ \theta_x & \Phi_x & \theta_\phi & -\Phi_\phi \end{array}\right] \begin{Bmatrix} x_s \\ y_s \\ \hline \phi_s \\ \theta_s \end{Bmatrix} \qquad \text{(D-1)}$$

Note that there are only eight distinct transfer functions. Due to the symmetrical form of eq. (D-1), the following transformation to complex response variables results in considerable simplification,

$$\begin{aligned} F &= F_{x\,s} + i\,F_{y\,s} \\ M &= M_{\phi\,s} + i\,M_{\theta\,s} \\ \xi &= x_s + i\,y_s \\ \eta &= \phi_s + i\,\theta_s \end{aligned} \qquad \text{(D-2)}$$

because, from eq. (D-1)

$$\begin{Bmatrix} F \\ M \end{Bmatrix} = \begin{bmatrix} F_\xi & F_\eta \\ M_\xi & M_\eta \end{bmatrix} \begin{Bmatrix} \xi \\ \eta \end{Bmatrix} \qquad \text{(D-3)}$$

where the complex transfer functions:

$$\begin{aligned} F_\xi &= X_x + i\,Y_x \\ F_\eta &= X_\phi + i\,Y_\phi \\ M_\xi &= \Phi_x + i\,\theta_x \\ M_\eta &= \Phi_\phi + i\,\theta_\phi \end{aligned} \qquad \text{(D-4)}$$

An analogous set of relationships can be written for forces and moments on the hub in the rotating coordinate system

$$\begin{Bmatrix} \overline{F} \\ \overline{M} \end{Bmatrix} = \begin{bmatrix} \overline{F}_\xi & \overline{F}_\eta \\ \overline{M}_\xi & \overline{M}_\eta \end{bmatrix} \begin{Bmatrix} \overline{\xi} \\ \overline{\eta} \end{Bmatrix} \qquad \text{(D-5)}$$

where a bar is used to indicate variables and parameters in the rotating coordinate system. The complex transfer functions in the non-rotating coordinate system can be calculated from transfer functions in the rotating coordinate system by means of the following theorem developed by J. H. Hill (Reference 2). (See Appendix II for derivation).

$$\begin{aligned} F_{\xi\,(s)} &= \overline{F}_{\xi\,(p)}\Big|_{p\,=\,s\,-\,i\omega} \\ F_{\eta\,(s)} &= F_{\eta\,(p)}\Big|_{p\,=\,s\,-\,i\omega} \\ &\text{Etc.} \end{aligned} \qquad \text{(D-6)}$$

where p is the complex frequency parameter in the rotating system and s is the complex frequency parameter in the stationary system. Thus, to obtain F_ξ, simply substitute $p = s - i\omega$ into $\overline{F}_\xi$.

Equation (C-4) indicates the form of the real transfer functions in rotating coordinates for a single blade. Writing out the terms in the matrix

$$\begin{Bmatrix} F_{x\,n} \\ F_{y\,n} \\ \hline M_{\phi\,n} \\ M_{\theta\,n} \end{Bmatrix} = \left[\begin{array}{cc|cc} \overline{X}_{x\,n} & \overline{X}_{y\,n} & \overline{X}_{\phi\,n} & \overline{X}_{\theta\,n} \\ \overline{Y}_{x\,n} & \overline{Y}_{y\,n} & \overline{Y}_{\phi\,n} & \overline{Y}_{\theta\,n} \\ \hline \overline{\Phi}_{x\,n} & \overline{\Phi}_{y\,n} & \overline{\Phi}_{\phi\,n} & \overline{\Phi}_{\theta\,n} \\ \overline{\theta}_{x\,n} & \overline{\theta}_{y\,n} & \overline{\theta}_{\phi\,n} & \overline{\theta}_{\theta\,n} \end{array}\right] \begin{Bmatrix} x_n \\ y_n \\ \hline \Phi_n \\ \theta_n \end{Bmatrix} \qquad \text{(D-7)}$$

For a single blade, symmetry such as that indicated by eq. (D-1) does not exist. Nevertheless, it is shown in Appendix II that, for the rotor as a whole,

$$\begin{aligned} F_{\xi\,(s)} &= \frac{n}{2}\left[\overline{X}_{x\,n} + \overline{Y}_{y\,n} + i(\overline{Y}_{x\,n} - \overline{X}_{y\,n})\right]_{p\,=\,s\,-\,i\omega} \\ F_{\eta\,(s)} &= \frac{n}{2}\left[\overline{X}_{\phi\,n} + \overline{Y}_{\theta\,n} + i(\overline{Y}_{\phi\,n} - \overline{X}_{\theta\,n})\right]_{p\,=\,s\,-\,i\omega} \\ &\text{Etc.} \end{aligned} \qquad \text{(D-8)}$$

where n is the number of blades. Thus, eqs. (D-8) and (C-4) provide a procedure for calculating transfer functions for the rotor in stationary coordinates from the equations of motion of a single blade.

Stability derivatives are defined by relationships of the sort

$$\begin{aligned} F &= f_\xi\,\xi + f_{\dot\xi}\,\dot\xi + f_{\bar\xi}\,\bar\xi + \ldots f_\eta\,\eta + f_{\dot\eta}\,\dot\eta + \ldots \\ M &= m_\xi\,\xi + m_{\dot\xi}\,\dot\xi + m_{\bar\xi}\,\bar\xi + \ldots m_\eta\,\eta + m_{\dot\eta}\,\dot\eta + \ldots \end{aligned} \qquad \text{(D-9)}$$

where f_ξ, $f_{\dot\xi}$, $f_{\bar\xi}$ ... m_ξ ... $m_{\bar\eta}$ etc. are stability derivatives.

Stability derivatives may be evaluated from the properties of the transfer functions at $s = 0$.

$$f_\xi = F_\xi(s)\Big|_{s=0}$$

$$f_{\dot\xi} = \frac{d}{ds} F_\xi(s)\Big|_{s=0} \qquad \text{(D-10)}$$

$$f_{\ddot\xi} = \frac{1}{2}\frac{d^2}{ds^2} F_\xi(s)\Big|_{s=0}$$

Etc.

Utilizing eq. (D-6) and the scaled frequency variable, $\bar p = p/\omega$

$$f_\xi = F_\xi(\bar p)\Big|_{\bar p=-i}$$

$$f_{\dot\xi} = \frac{1}{\omega}\frac{d}{d\bar p}\bar F_\xi(\bar p)\Big|_{\bar p=-i} \qquad \text{(D-11)}$$

$$f_{\ddot\xi} = \frac{1}{2\omega^2}\frac{d^2}{d\bar p^2}\bar F_\xi(\bar p)\Big|_{\bar p=-i}$$

In the present instance only the static and first derivative terms will be computed. The third term yields the effective mass properties of the rotor. It will be assumed in evaluating mass properties that the rotor is a concentrated mass located at its center of gravity.

The real stability derivatives are obtained directly from the real and imaginary parts of the complex stability derivatives

$$f_\xi = f_x + i f_y$$
$$f_{\dot\xi} = f_{\dot x} + i f_{\dot y} \qquad \text{(D-12)}$$

We now turn to the evaluation of rotor transfer functions by means of eq. (D-8), substituting from eq. (C-4) and making use of the terms tabulated in Appendix I.

$$F_\xi = \frac{n}{2} M_b \omega^2 \Big[\bar H_{xx} + \bar H_{yy} + i(\bar H_{yx} - \bar H_{xy}) + \frac{\sin^2\beta_c}{\ell_{o2}^2(1+\bar p^2+\omega_b^2+2\zeta_b\bar p)} \qquad \text{(D-13)}$$
$$(H_x^* + i H_y^*)(B_x^* - i B_y^*)\Big]_{\bar p = \frac{s}{\omega} - i}$$

The total thrust of the rotor is, under the assumption of constant coning angle,

$$T_o = n m_b \omega^2 \ell_{1o} \sin\beta_c \cos\beta_c \qquad \text{(D-14)}$$

so that eq. (D-13) may be written as:

$$F_\xi = \frac{T_o}{2}\left\{\frac{1}{\ell_{10}\sin\beta_c\cos\beta_c}\bar H_{\xi\dot\xi} + \frac{\tan\beta_c}{\ell_{10}\ell_{02}^2} H^*_{\xi\dot\xi}\right\}_{\bar p = \frac{s}{\omega} - i} \qquad \text{(D-15)}$$

where

$$\bar H_{\xi\xi} = \bar H_{xx} + \bar H_{yy} + i(\bar H_{yx} - \bar H_{xy}) \qquad \text{(D-16)}$$

$$H^*_{\xi\xi} = \frac{(H_x^* + i H_y^*)(B_x^* - i B_y^*)}{1 + \bar p^2 + \bar\omega_b^2 + 2\zeta_n \bar p} \qquad \text{(D-17)}$$

The rotor derivatives f_ξ and $f_{\dot\xi}$ are obtained by applying eq. (D-11) to eq. (D-15). Both $\bar H_{\xi\xi}$ and $B_x^* - i B_y^*$ vanish for $\bar p = -i$, so that:

$$f_\xi = 0$$

and

$$f_{\dot\xi} = \frac{T_o}{2\omega}\left\{\frac{1}{\ell_{10}\sin\beta_c\cos\beta_c}\frac{d}{d\bar p}(\bar H_{\xi\xi}) + \frac{\tan\beta_c}{\ell_{10}\ell_{02}^2}\frac{H_x^* + i H_y^*}{\bar\omega_b^2 - 2 i\zeta_b}\frac{d}{d\bar p}(B_x^* - i B_y^*)\right\}_{\bar p=-i} \qquad \text{(D-18)}$$

In like manner, $m_\xi = 0$,

and

$$m_{\dot\xi} = \frac{T}{2\omega}\left\{\frac{1}{\ell_{10}\sin\beta_c\cos\beta_c}\frac{d}{d\bar p}(\bar H_{\eta\xi}) + \frac{\tan\beta_c}{\ell_{10}\ell_{02}^2}\frac{H_\phi^* + i H_\theta^*}{\bar\omega_b^2 - 2 i\zeta_b}\frac{d}{d\bar p}(B_x^* - i B_y^*)\right\}_{\bar p=-i} \qquad \text{(D-19)}$$

The vanishing of f_ξ and m_ξ is an expression of the fact that the location of the hub in space is immaterial to the forces on the hub. The static derivatives of angular orientation are

$$f_\eta = \frac{T_o}{2}\left\{\frac{1}{\ell_{10}\sin\beta_c\cos\beta_c}\bar H_{\xi\eta} + \frac{\tan\beta_c}{\ell_{10}\ell_{02}^2} H^*_{\xi\eta}\right\}_{\bar p=-i} \qquad \text{(D-20)}$$

and

$$m_n = \frac{T_o}{2}\left\{\frac{1}{\ell_{10}\sin\beta_c\cos\beta_c}\bar H_{\eta\eta} + \frac{\tan\beta_c}{\ell_{10}\ell_{02}^2} H^*_{\eta\eta}\right\}_{\bar p=-i} \qquad \text{(D-21)}$$

where

$$H^*_{\xi\eta}\Big|_{\bar p=-i} = \frac{(H_x^* + i H_y^*)(B_\phi^* - i B_\theta^*)}{\bar\omega_b^2 - 2 i\zeta_b}\Big|_{\bar p=-i} \qquad \text{(D-22)}$$

and

$$H^*_{\eta\eta}\Big|_{\bar{p}=-i} = \frac{(H^*_\phi + iH^*_\theta)(B^*_\phi - iB^*_\theta)}{\bar{\omega}_b^2 - 2i\zeta_b}\Bigg|_{\bar{p}=-i} \qquad \text{(D-23)}$$

The derivatives of angular velocity are

$$f_{\dot{\eta}} = \frac{T_o}{2\omega}\left\{\frac{1}{\ell_{10}\sin\beta_c\cos\beta_c}\frac{d}{d\bar{p}}(\bar{H}_{\xi\eta}) + \frac{\tan\beta_c}{\ell_{10}\ell_{02}^2}H^*_{\xi\eta}\left[\frac{\frac{d}{d\bar{p}}(H^*_x + iH^*_y)}{H^*_x + iH^*_y} + \frac{\frac{d}{d\bar{p}}(B^*_x - iB^*_\theta)}{B^*_\phi - iB^*_\theta} - \frac{2\zeta_b - 2i}{\bar{\omega}_b^2 - 2i\zeta_b}\right]\right\}_{\bar{p}=-1} \qquad \text{(D-24)}$$

and

$$m_{\dot{\eta}} = \frac{T_o}{2\omega}\left\{\frac{1}{\ell_{10}\sin\beta_c\cos\beta_c}\frac{d}{d\bar{p}}(\bar{H}_{\eta\eta}) + \frac{\tan\beta_c}{\ell_{10}\ell_{02}^2}H^*_{\eta\eta}\left[\frac{\frac{d}{d\bar{p}}(H^*_\phi + iH^*_\theta)}{H^*_\phi + iH^*_\theta} + \frac{\frac{d}{d\bar{p}}(B^*_\phi - iB^*_\theta)}{B^*_\phi - iB^*_\theta} - \frac{2\zeta_b - 2i}{\bar{\omega}_b^2 - 2i\zeta_b}\right]\right\}_{\bar{p}=-i} \qquad \text{(D-25)}$$

All of the factors required in these equations for the evaluation of rotor derivatives are listed in Appendix III in terms of physical rotor parameters.

The rotor derivatives may be related to dimensionless derivative coefficients by the following formulas

$$\begin{aligned} f_\xi &= 0 & f_{\dot{\xi}} &= \frac{T_o}{\omega\ell}C_{\dot{\xi}} \\ f_\eta &= T_o C_\eta & f_{\dot{\eta}} &= \frac{T_o}{\omega\ell}C_{\dot{\eta}} \\ m_\xi &= 0 & m_{\dot{\xi}} &= \frac{T_o}{\omega}D_{\dot{\xi}} \\ m_\eta &= T_o\ell D_\eta & m_{\dot{\eta}} &= \frac{T_o\ell}{\omega}D_{\dot{\eta}} \end{aligned} \qquad \text{(D-26)}$$

where ℓ is the length of the blade outboard of the flapping hinge (see Figure 8).

The real and imaginary parts of the dimensionless derivative coefficients are plotted in Figures 9 and 10 for a uniform mass distribution along the span of the blade. An immediate observation from these figures is that the rotor derivatives vary through wide ranges as functions of tip speed, coning angle and flap hinge offset.

$C_{Y\phi}$ (= I. P. C_Y) is the directional stability of the rotor. For a conventional subsonic helicopter the value of this derivative is -1.0 corresponding to neutral directional stability. Values greater than -1.0 yield positive directional stability with respect to the flight path. It may be observed in Figures 9c and 10c that the directional stability is essentially zero for zero flap hinge offset, and that it increases with increasing coning angle and decreases with increasing tip speed ratio.

$C_{\dot{Y}\phi}$ is the conventional pitch damping derivative for a rotor without flap-hinge offset and for positive values the damping in pitch is positive (stable). It may be observed in Figures 9d and 10d that large coning angles and values of b/ℓ near .05 produce negative damping in pitch. This result is offset by the large negative values of $D_{\dot{\phi}\dot{\phi}}$ in the same neighborhood (Figures 9f and 10f).

It will also be observed that surprisingly small values of flap-hinge offset have a large effect on all derivatives. The damping of the rotor is very small at low tip speed ratios so that the detuning effect of flap hinge offset is significant even for very small values of this parameter. No conclusions regarding dynamic stability of the vehicle can be made from the rotor derivatives alone except to say that stability may be expected to vary widely at points along a reentry trajectory that have different tip-speed ratios and coning angles.

E. Lateral Stability in Axial Flight

It is assumed that the vehicle to which the rotor is attached is rigid, is doubly symmetrical, and has the same moment of inertia about two lateral axes. The equations of motion expressed in terms of hub motions are

$$m(\ddot{x}_s - z\ddot{\theta}_s) = F_{xs} \qquad \text{(E-1)}$$

$$m(\ddot{y}_s + z\ddot{\phi}_s) = F_{ys} \qquad \text{(E-2)}$$

$$(I_{cg} + mz^2)\ddot{\phi}_s + T_o z\phi_s + mz\ddot{y}_s = M_{\phi s} \qquad \text{(E-3)}$$

$$(I_{cg} + mz^2)\ddot{\theta}_s + T_o z\theta_s - mz\ddot{x}_s = M_{\theta s} \qquad \text{(E-4)}$$

where

m = mass of the vehicle

z = distance measured aft, from c.g. to hub

I_{cg} = pitching moment of inertia about the c.g.

T_o = total thrust of the rotor

Introduce the complex variables defined in eq. (D-2)

$$m\ddot{\xi} + imz\ddot{\eta} = F \qquad \text{(E-5}$$

$$(I_{cg} + mz^2)\ddot{\eta} + T_o z\eta - imz\ddot{\zeta} = M \qquad \text{(E-6}$$

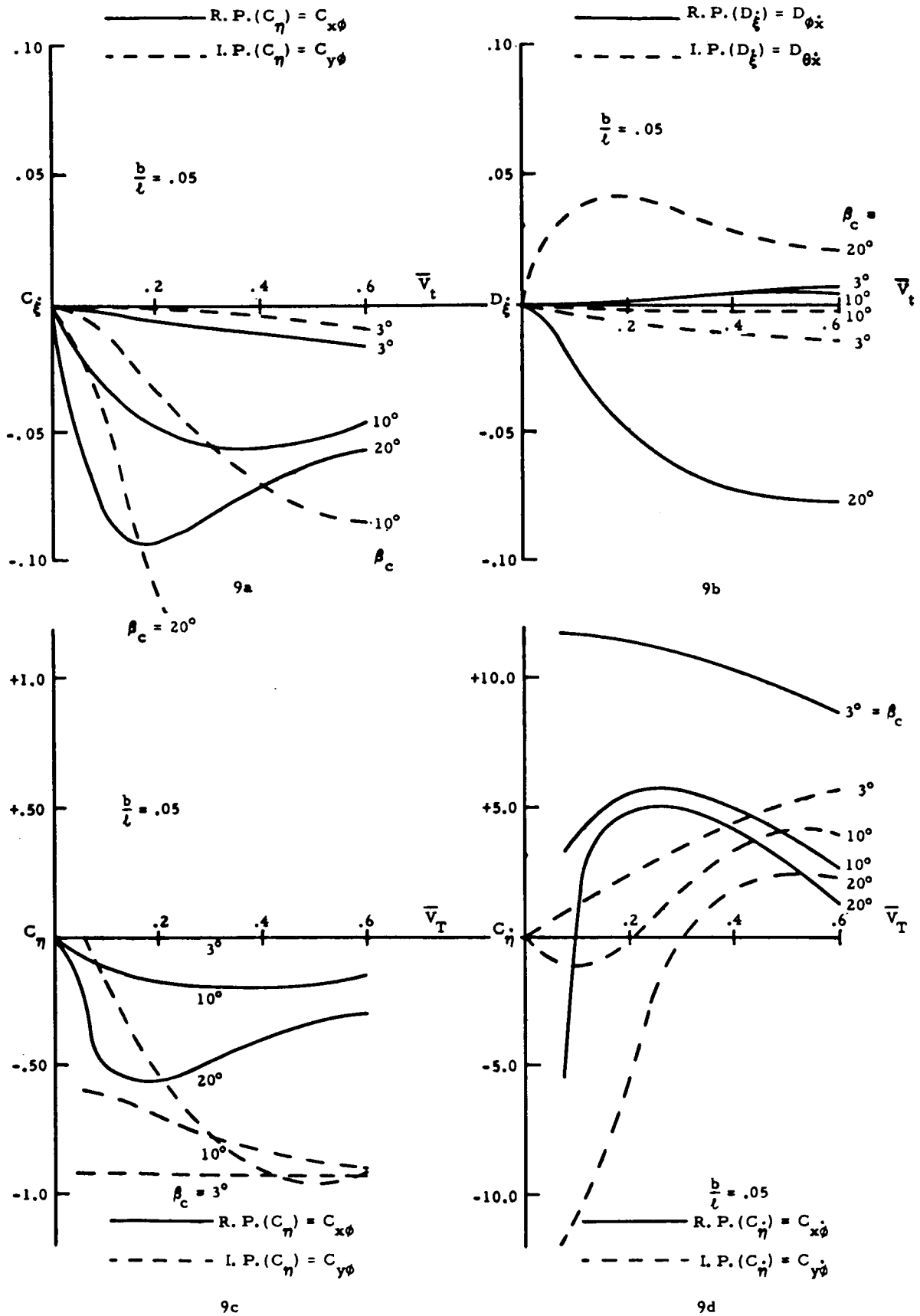

Figure 9. Rotor Derivatives Plotted vs. Tip-Speed Ratio.

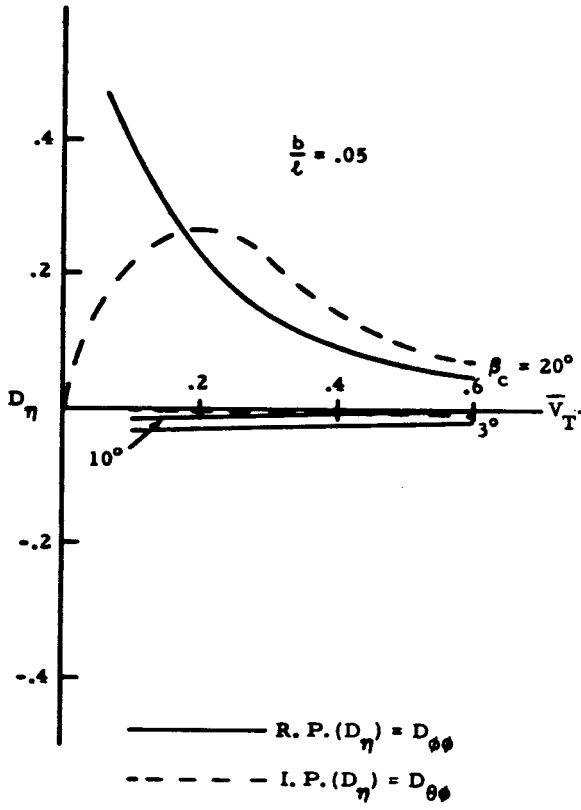
.4
.2
-.2
-.4
$\frac{b}{\ell}$ = .05
β_c = 20°
.2
.4
.6
D_η
$\bar{V}_T$
10°
3°
R. P. $(D_\eta) = D_{\phi\phi}$
I. P. $(D_\eta) = D_{\theta\phi}$

9e

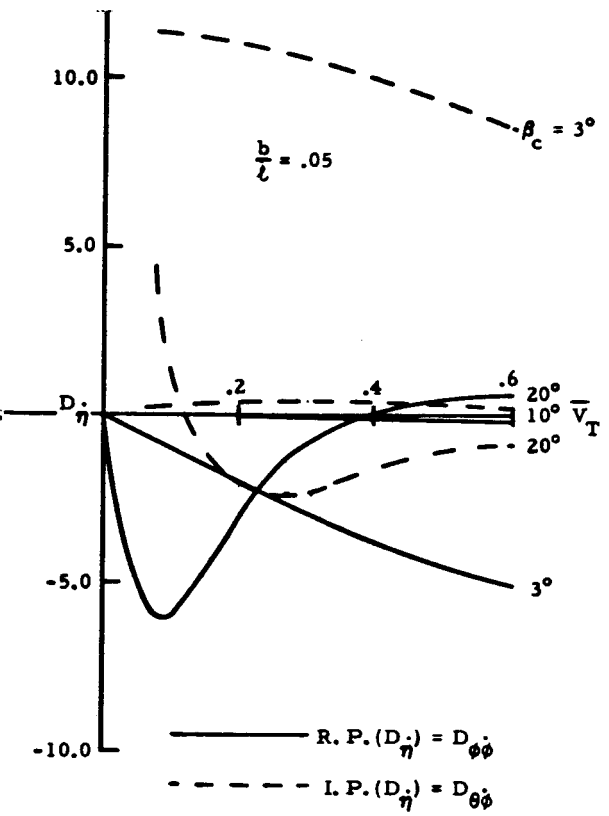
10.0
5.0
-5.0
-10.0
$\frac{b}{\ell}$ = .05
β_c = 3°
.2
.4
.6
$D_{\dot\eta}$
$\bar{V}_T$
20°
10°
20°
3°
R. P. $(D_{\dot\eta}) = D_{\phi\dot\phi}$
I. P. $(D_{\dot\eta}) = D_{\theta\dot\phi}$

9f

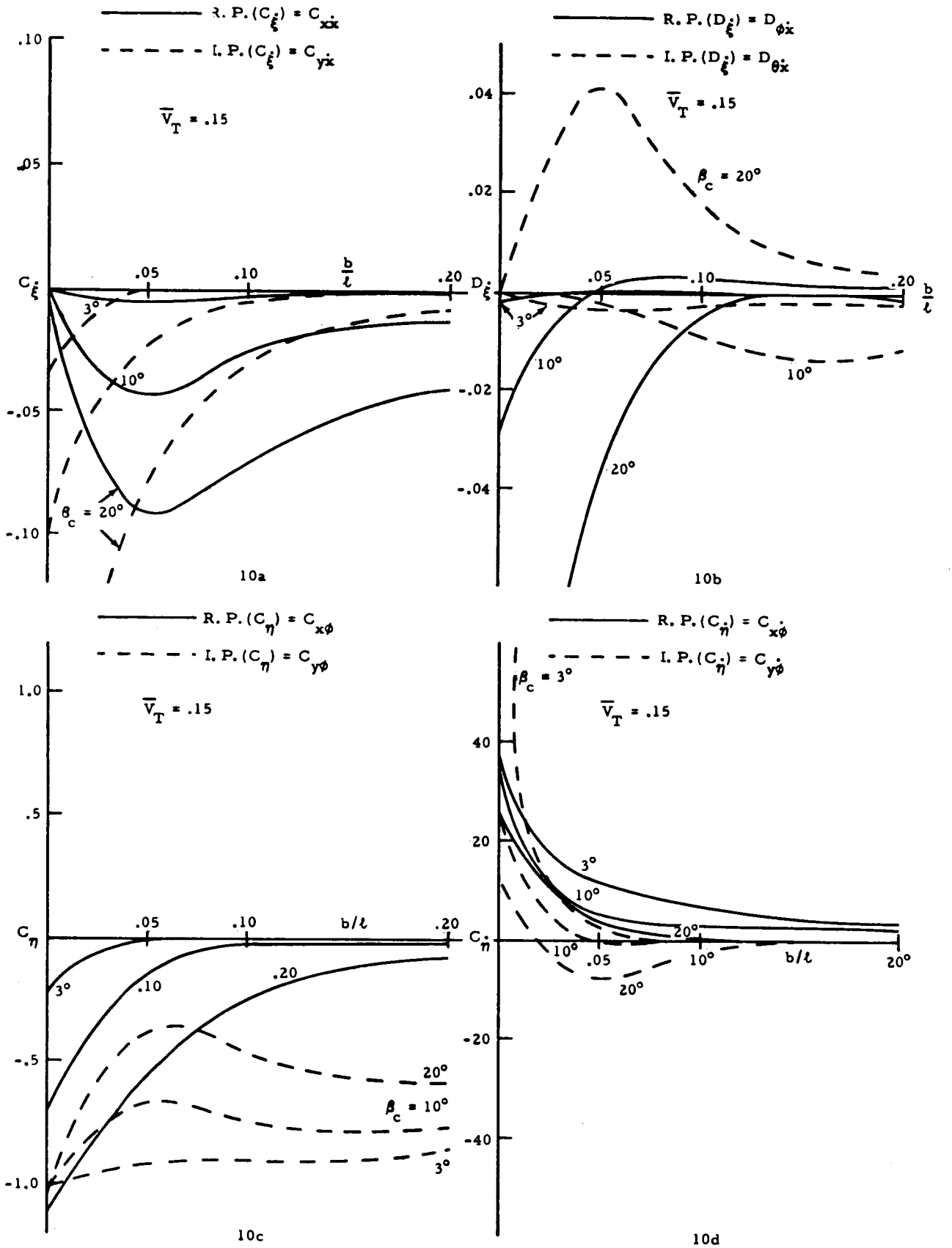

Figure 10. Rotor Derivatives Plotted vs. Flap Hinge Offset.

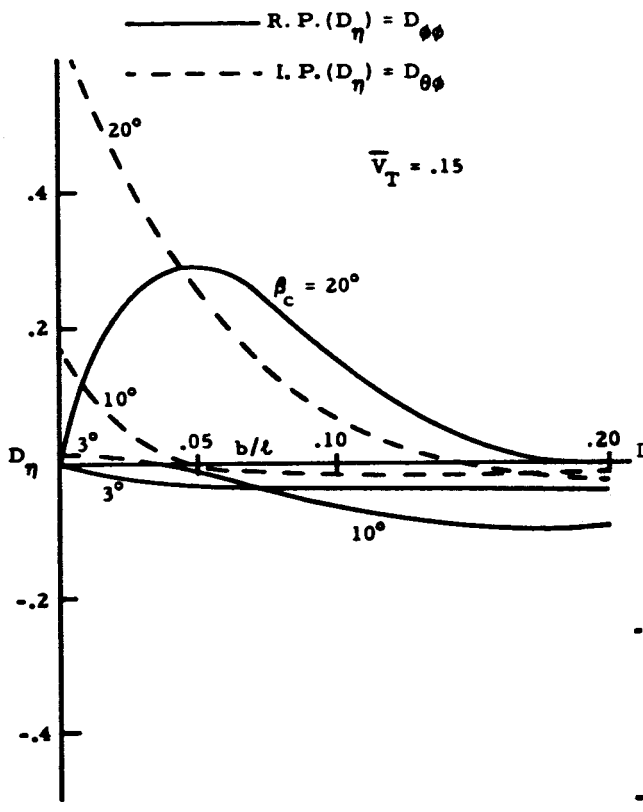
R. P. $(D_\eta) = D_{\phi\phi}$
I. P. $(D_\eta) = D_{\theta\phi}$
$\bar{V}_T = .15$
$\beta_c = 20°$
20°
10°
3°
D_η
b/ℓ
.4
.2
-.2
-.4
.05
.10
.20

10e

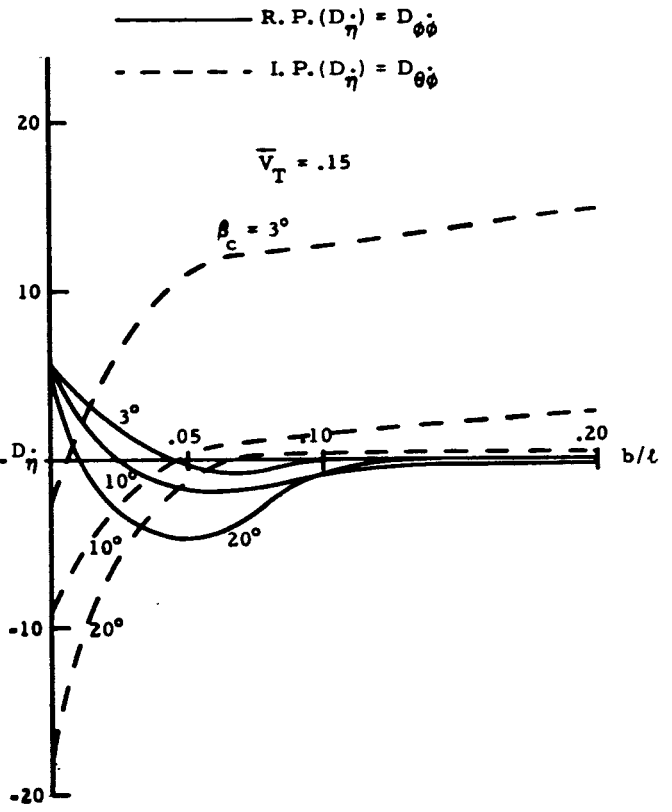
R. P. $(D_{\dot\eta}) = D_{\phi\dot\phi}$
I. P. $(D_{\dot\eta}) = D_{\theta\dot\phi}$
$\bar{V}_T = .15$
$\beta_c = 3°$
3°
10°
20°
$D_{\dot\eta}$
b/ℓ
20
10
-10
-20
.05
.10
.20

10f

Replace the force and moment due to the hub by the expressions in eq. (D-9), truncated to include the first derivative terms. Then, in matrix form, with $s \equiv \frac{d}{dt}$,

$$\left[\begin{array}{c|c} ms - f_{\dot{\xi}} & imzs^2 - f_\eta - sf_{\dot{\eta}} \\ \hline imzs - m_{\dot{\xi}} & (I_{cg} + mz^2)s^2 + T_o z - m_\eta - sm_{\dot{\eta}} \end{array}\right]\left\{\begin{array}{c} \dot{\xi} \\ \hline \eta \end{array}\right\} = 0 \qquad \text{(E-7)}$$

The determinant of this set of equations is a cubic equation which can be written in the following form

$$B_3\bar{s}^3 + B_2\bar{s}^2 + B_1\bar{s} + B_o = 0 \qquad \text{(E-8)}$$

where $\bar{s} = s/\omega$ and the coefficients are functions of the derivative coefficients defined in eq. (D-26) and the following dimensionless parameters

$$\bar{K}^2 = \frac{I_{cg}}{m\ell^2}$$

$$\bar{z} = z/\ell \quad ; \quad \bar{g} = \frac{T_o}{m\omega^2\ell}$$

the coefficients are:

$$\begin{aligned} B_3 &= \bar{K}^2/\bar{g} \\ B_2 &= -\left[D_{\dot{\eta}} + i\bar{z}(C_{\dot{\eta}} - D_{\dot{\xi}}) + (\bar{z}^2 + \bar{K}^2)C_{\dot{\xi}}\right] \\ B_1 &= -\left[D_\eta + \bar{z}(iC_\eta - 1) + \bar{g}(C_{\dot{\xi}} D_{\dot{\eta}} - D_{\dot{\xi}} C_{\dot{\eta}})\right] \\ B_0 &= -\bar{g}\left[C_\xi + C_\eta D_{\dot{\xi}} - D_\eta C_{\dot{\xi}}\right] \end{aligned} \qquad \text{(E-9)}$$

A physical interpretation of the parameter $\bar{g}$ is that it is equal to the ratio of the deceleration of the vehicle to the centripetal acceleration at a point near the tip of a rotor blade. The derivative coefficients are functions of the following rotor parameters

$\bar{V}_T$	tip speed ratio
β_c	coning angle
b/ℓ	flap hinge offset
$m'_{(s)}$	blade mass distribution

Thus, for the simplified system considered here, vehicle stability is a function of seven parameters, four of which are fixed for a given vehicle, (b/ℓ, $\bar{K}$, $\bar{z}$ and blade mass distribution) and three of which depend on operating conditions ($\bar{V}_T$, β_c and $\bar{g}$).

For a given reentry trajectory $\bar{V}_T$, β_c and $\bar{g}$ can be determined at points along the trajectory, producing curves of the roots of the stability equation as a function of time.

For a blade with uniform spanwise mass distribution and an aerodynamic chord that satisfies the uniform coning angle assumption, eq. (C-1), the tip speed ratio may be put into the following forms

$$\bar{V}_T = 2\left[g\ell \cdot \rho A \cdot \frac{m}{m_r} \frac{\cos^2\beta_c}{\sin\beta_c}\left(\frac{b}{\ell} + \frac{1}{2}\cos\beta_c\right)\right]^{1/2} \qquad \text{(E-10)}$$

$$\bar{V}_T = \frac{2}{U}\left[g\ell \cdot \frac{D}{W} \cdot \frac{m}{m_r} \frac{b/\ell + \frac{1}{2}\cos\beta_c}{\sin\beta_c \cos\beta_c}\right]^{1/2} \qquad \text{(E-11)}$$

where A is the total area of the rotor (number of blades times blade area), W is the total weight of the vehicle and m_r is the total mass of the rotor. The first expression shows that, for a constant coning angle trajectory, the tip speed ratio increases as the square root of the density. The second expression shows that maximum tip speed occurs at maximum deceleration.

Under the same assumptions the deceleration parameter is

$$\bar{g} = \frac{m_r}{m}\sin\beta_c \cos\beta_c\left(\frac{b}{\ell} + \frac{1}{2}\cos\beta_c\right) \qquad \text{(E-12)}$$

Thus for a constant coning angle trajectory, only the tip speed ratio depends on trajectory data and a plot of stability vs. tip speed ratio may easily be interpreted as a plot of stability vs. time.

The stability of a family of typical reentry vehicles will be investigated. These vehicles will have the same coning angle and will differ only with regard to the rotor mass ratio, m_r/m. The fixed parameters for these vehicles are

$$b/\ell = .05, \quad \bar{z} = .25, \quad \bar{K}^2 = .03, \quad \beta_c = 10^\circ.$$

The following table gives the values of $\bar{g}$ and the associated rotor mass ratios for which data will be obtained

$\bar{g}$	$\frac{m_r}{m}$
.002	.0216
.004	.0432
.008	.0863

Thus the weight of the rotor blades is assumed to vary between 2.0% and 8.6% of the total vehicle weight. The reasonableness of the assumed coning angle will be checked by computing the tip speed at maximum deceleration from eq. (E-11). Assume m_r/m is .05, that the blade length is 100 ft., and that the maximum deceleration is 10 g's. Then

$$V_T = 2\left[32.2 \times 100 \times 10 \times \frac{1}{.05} \times 3.16\right]^{\frac{1}{2}} = 2850 \text{ ft/sec}$$

which is within the capability of high strength

materials. The axial velocity under these conditions will be assumed to be 16,000 ft/sec which is about 2/3 of orbital velocity. Thus the tip speed ratio is

$$\overline{V}_T = \frac{2850}{16000} = .178$$

Since the tip speed ratio depends on atmospheric density, eq. (E-10), the tip speed ratio will be lower at higher altitudes and high at lower altitudes. A range of tip speed ratios from .075 to .600 has been selected for investigation.

The results are plotted in Figures 11a, 11b and 11c for each of the three roots of the stability equation. The magnitudes of the three roots are roughly in the proportion 100/10/1.0. The medium root is unstable and the small root is stable for all conditions analyzed. The large root is unstable for the smaller values of $\overline{V}_T$.

The wide separation in magnitude of the three roots implies that each root may be evaluated approximately from the ratio of successive terms in the stability equation. The instability of the large root for small $\overline{V}_T$ may, by this means, be traced to the negative value of the pitch damping coefficient, $C_{y\dot{\phi}}$, (see Figure 9d).

The force derivative of lateral velocity, $C_{\dot{\xi}}$, dominates the constant term, B_0, in eq. (E-9), so that the small root is closely associated with lateral translational velcoity of the vehicle. This root is very small and is stable, indicating that lateral translation may be considered to be virtually undamped.

The instability of the medium root is related to the phase relationship between C_η and $C_{\dot{\eta}}$.

It should be pointed out that one of the three roots of a conventional hovering helicopter is normally unstable but that the instability is acceptable because the frequency and time to double amplitude (5–20 sec) are within the control capability of the pilot. The instabilities indicated in Figure 11 are somewhat more severe. For example, if the real part of the root is .03, amplitude is doubled every 3.7 revolutions. Thus, for a rotor speed of 3.7 rev/sec, the amplitude is doubled in one second.

Although such an instability is beyond the capability of a human pilot, it seems quite probable that an electronic autopilot could control an instability of this order of severity. In addition it is certain that other values of rotor parameters can be found for which the instabilities are moderated or eliminated entirely. The instability of the high frequency root should be corrected in this manner.

Another means of improving stability that may prove to be effective is to add auxiliary aerodynamic surfaces to the vehicle that will increase the imaginary parts of C_η and $C_{\dot{\eta}}$.

It seems likely, at this time, that, in view of the wide range of operating parameters during atmospheric entry, some form of black-box stabilization will be necessary.

References for Part II

[1] Ham, Norman D., "An Experimental and Theoretical Investigation of a Supersonic Rotating Decelerator," Journ. of American Helicopter Society, Vol. 8, #1, January 1963.

[2] Hill, J. H. "A Study of Hovering Stability of Single-Rotor Helicopters," Computer Engineering Associates Report ES189, September 1962.

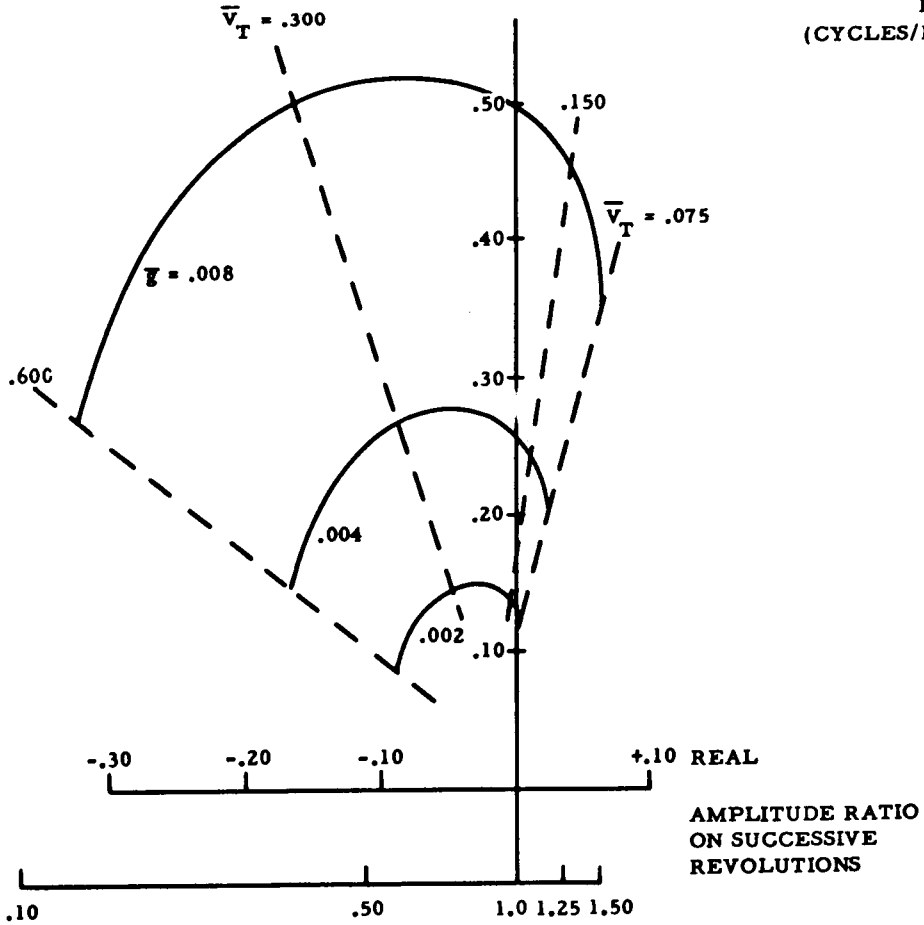

Figure 11a. Large Root of Stability Equation

$\beta_c = 10°$, $b/\ell = .05$, $\overline{z} = .25$, $\overline{K}^2 = .03$.

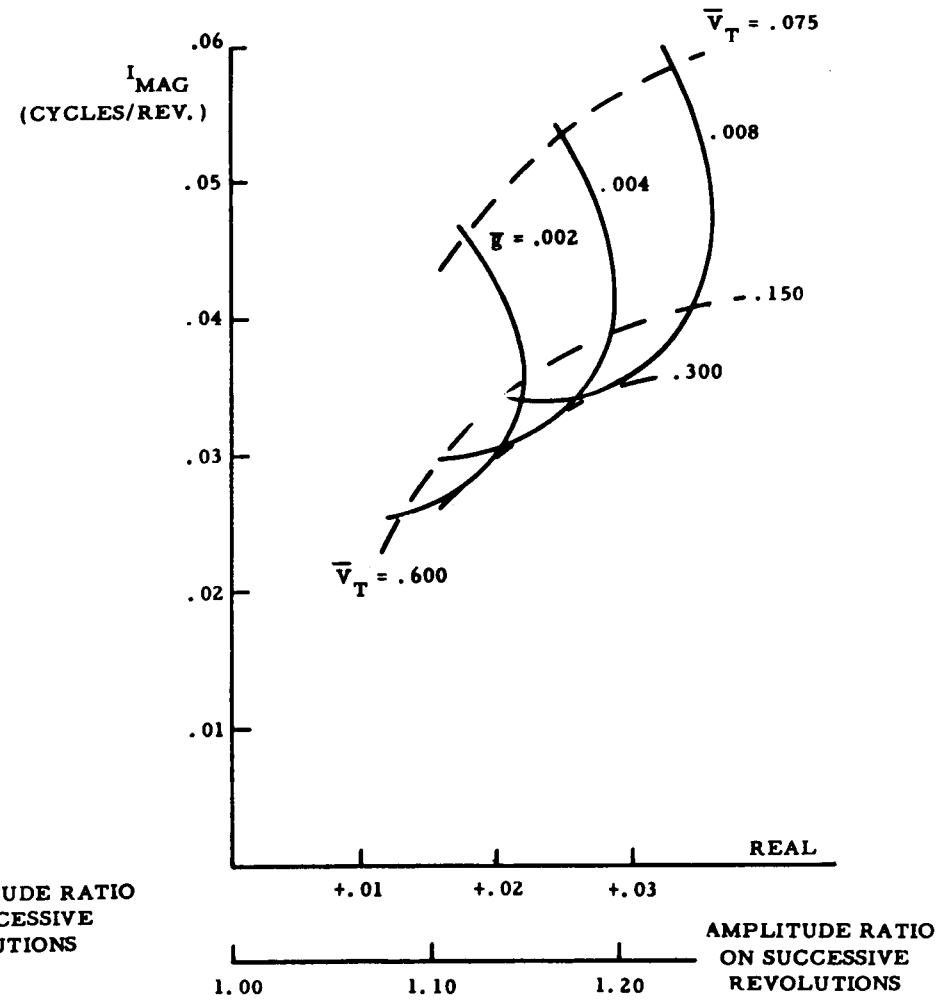

Figure 11b. Medium Root of Stability Equation

$\beta_c = 10°$, $\frac{b}{\ell} = .05$, $\overline{z} = .25$, $\overline{K}^2 = .03$.

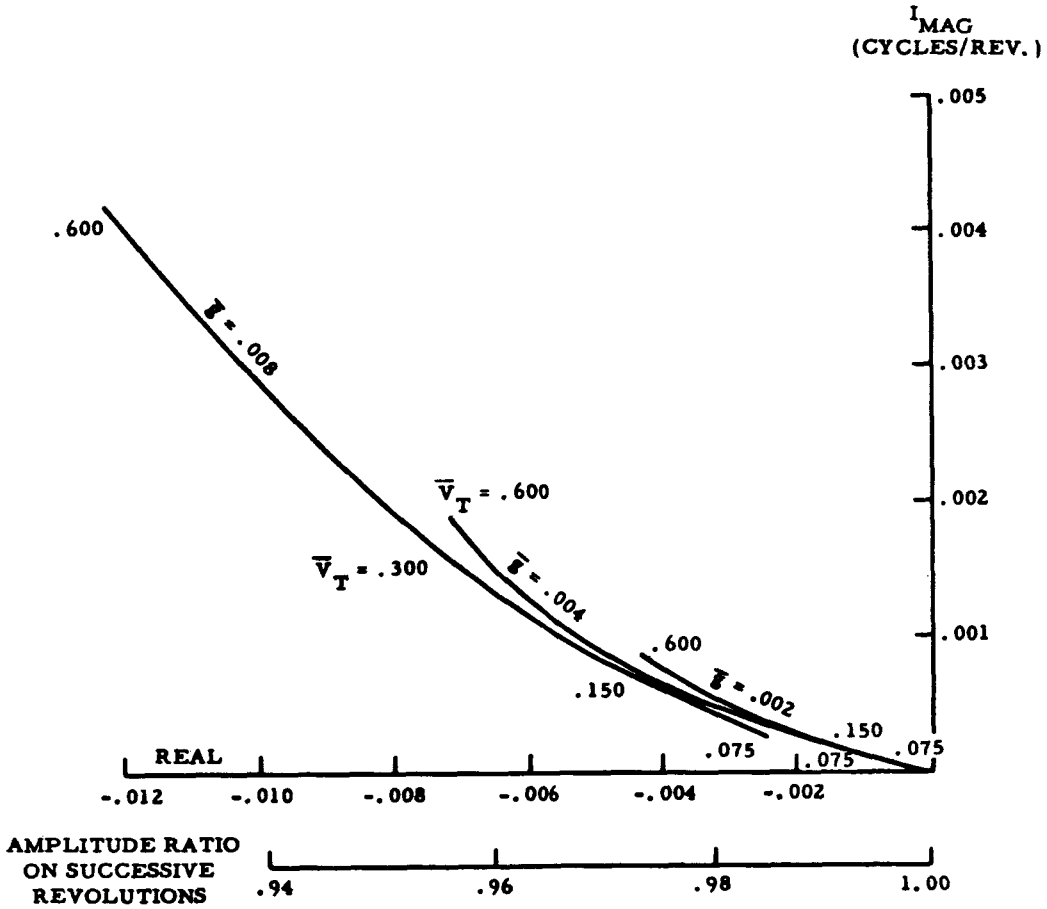

Figure 11c. Small Root of Stability Equation
$\beta_c = 10^\circ$, $\frac{b}{\ell} = .05$, $\bar{\mu} = .25$, $\bar{K}^2 = .03$.

Terms in the Equation of Blade Motion (Eq. C-3)

The following special symbols are employed

$$\overline{p} = \frac{1}{\omega}\frac{d}{dt}$$

$$\overline{V}_t = \frac{2\omega \ell_{10}}{V}$$

A speed ratio which is, for a blade with uniform mass distribution, equal to the ratio of tip speed to axial velocity.

$$\overline{\omega}_b^2 = \left(\frac{\omega_b}{\omega}\right)^2 =$$

$$\frac{b\ell_{01}}{\ell_{02}^2}(\cos\beta_c + 2\sin\beta_c \tan\beta_c)$$

$$\zeta_b = \overline{V}_t \cdot \frac{\ell_{12}^3}{2\ell_{10}\ell_{02}^2} \cdot \tan\beta_c$$

$$\ell_{01} = \frac{1}{m_b}\int_o^\ell m s\, ds$$

$$\ell_{02} = \frac{1}{m_b}\int_o^\ell m s^2\, ds$$

$$\ell_{10} = \frac{1}{m_b}\int_o^\ell m r\, ds$$

$$\ell_{11}^2 = \frac{1}{m_b}\int_o^\ell m r s\, ds$$

$$\ell_{12}^3 = \frac{1}{m_b}\int_o^\ell m r s^2\, ds$$

$$\ell_{21}^3 = \frac{1}{m_b}\int_o^\ell m r^2 s\, ds$$

The coefficients in eq. (C-3) are tabulated below. Note that $[H_\beta]$ is a column matrix and $[B_n]$ is a row matrix.

$$[H_n] = m_b \omega^2 [\overline{H}]$$

$$\overline{H}_{xx} = 1 - \overline{p}^2$$

$$\overline{H}_{xy} = 2\overline{p}$$

$$\overline{H}_{x\phi} = 0$$

$$\overline{H}_{x\theta} = \ell_{10}\sin\beta_c + (1 - \overline{p}^2)\ell_{01}\sin\beta_c$$

$$\overline{H}_{yx} = -2\overline{p} - \overline{V}_t \tan\beta_c \sin^2\beta_c$$

$$\overline{H}_{yy} = 1 - \overline{p}^2 - \overline{V}_t \overline{p} \tan\beta_c \sin^2\beta_c$$

$$\overline{H}_{y\phi} = \overline{V}_t\, b\, \overline{p} \sin^2\beta_c$$

$$\overline{H}_{y\theta} = -2\overline{p}\,\ell_{01}\sin\beta_c - \overline{V}_t \sin\beta_c \tan\beta_c \left(\frac{\ell_{11}^2}{\ell_{10}} + b\cos\beta_c\right)$$

$$\overline{H}_{\phi x} = \overline{V}_t\, b \sin^2\beta_c$$

$$\overline{H}_{\phi y} = \overline{V}_t\, b\, \overline{p} \sin^2\beta_c$$

$$\overline{H}_{\phi\phi} = -\overline{p}^2 b^2 - \ell_{10} b \cos^2\beta_c - \overline{V}_t\, b^2\, \overline{p} \sin\beta_c \cos\beta_c$$

$$\overline{H}_{\phi\theta} = \overline{V}_t\, b \sin\beta_c \left(\frac{\ell_{11}^2}{\ell_{10}} + b\cos\beta_c\right)$$

$$H_{\theta x} = (1 - \overline{p}^2)\ell_{01}\sin\beta_c$$

$$H_{\theta y} = 2\overline{p}\,\ell_{01}\sin\beta_c$$

$$H_{\theta\phi} = 0$$

$$H_{\theta\theta} = \left[\ell_{02}^2(1 - \overline{p}^2) + \ell_{11}^2(1 - \cos\beta_c)\right]\sin^2\beta_c$$

$$[H_\beta] = m_b \omega^2 \sin\beta_c \quad [H^*]$$

$$H^*_x = -2\overline{p}\,\ell_{01}$$

$$H^*_y = (\overline{p}^2 - 1)\ell_{01} + \ell_{01}(2\tan\beta_c \sin\beta_c - \cos\beta_c) + \overline{V}_t \cdot \overline{p}\frac{\ell_{11}^2}{\ell_{10}} \tan\beta_c$$

$$H^*_\phi = -\overline{p}^2 b\,\ell_{01}\,\mathrm{ctn}\beta_c - 3b\,\ell_{01}\sin\beta_c - \overline{V}_t\,\overline{p} \cdot \frac{b\,\ell_{11}^2}{\ell_{10}}$$

$$H^*_\theta = -2\overline{p}\,\ell_{02}^2 \sin\beta_c$$

$$[B_n] = m_b \omega^2 \sin\beta_c \cdot [B^*]$$

$$B^*_x = 2\bar{p}\, \ell_{01} + \bar{V}_t \frac{\ell_{11}^2}{\ell_{10}} \tan\beta_c$$

$$B^*_y = (\bar{p}^2 - 1)\ell_{01} + \bar{V}_t \bar{p} \frac{\ell_{11}^2}{\ell_{10}} \tan\beta_c$$

$$B^*_\phi = -\bar{p}^2 b\, \ell_{01} \operatorname{ctn}\beta_c - \bar{V}_t \bar{p}\, b \frac{\ell_{11}^2}{\ell_{10}}$$

$$B^*_\theta = 2\bar{p}\, \ell_{02}^2 \sin\beta_c + \bar{V}_t \left(\frac{\ell_{21}^3}{\ell_{10}} + \frac{\ell_{12}^3}{\ell_{10}} \sin\beta_c \tan\beta_c\right)$$

$$B_\beta = -m_b \omega^2 \ell_{02}^2 \left[1 + \bar{p}^2 + \bar{\omega}_b^2 + 2\zeta_b \bar{p}\right]$$

APPENDIX II

Derivation of Hill's Rotary Transformation

Theorem

From Figure 1 the forces and motions in the stationary and rotating coordinate systems are related by

$$\begin{Bmatrix} x \\ y \end{Bmatrix} = \begin{bmatrix} \cos\psi & \sin\psi \\ -\sin\psi & \cos\psi \end{bmatrix} \begin{Bmatrix} x_s \\ y_s \end{Bmatrix} \tag{II-1}$$

$$\begin{Bmatrix} F_{x_s} \\ F_{y_s} \end{Bmatrix} = \begin{bmatrix} \cos\psi & -\sin\psi \\ \sin\psi & \cos\psi \end{bmatrix} \begin{Bmatrix} F_x \\ F_y \end{Bmatrix} \tag{II-2}$$

Define

$$\left.\begin{aligned} \bar{\xi} &= x + iy & \bar{F} &= F_x + iF_y \\ \xi &= x_s + iy_s & F &= F_{x_s} + iF_{y_s} \end{aligned}\right\} \tag{II-3}$$

Then

$$\bar{\xi} = x_s(\cos\psi - i\sin\psi) + y_s(\sin\psi + i\cos\psi) = \xi e^{-i\psi} \tag{II-4}$$

and

$$F = \bar{F} e^{i\psi} \tag{II-5}$$

It is shown in Section D that, due to the symmetry of the rotor in axial flight, there exists a complex transfer function such that

$$F = F_\xi(s) \cdot \xi \tag{II-6}$$

It is assumed that there exists a corresponding transfer function when the variables are expressed in rotating coordinates

$$\bar{F} = \bar{F}_\xi(p)\, \bar{\xi} \tag{II-7}$$

Consider a homogeneous solution of the equations of motion such that

$$\left.\begin{aligned} \xi &= \xi_o e^{\alpha t} \\ \text{and} \qquad F &= F_o e^{\alpha t} \end{aligned}\right\} \tag{II-8}$$

where α is real or complex. Then from eq. (II-6) and the properties of a linear derivative operator

$$F_o = F_\xi(\alpha)\, \xi_o \tag{II-9}$$

From eq. (II-4), and $\psi = \omega t$

$$\bar{\xi} = \xi_o e^{(\alpha - i\omega)t} \tag{II-10}$$

and

$$\bar{F} = \bar{F}_\xi(\alpha - i\omega)\xi_o e^{(\alpha - i\omega)t} \tag{II-11}$$

From eq. (II-5)

$$F = \bar{F}_\xi(\alpha - i\omega)\xi_o e^{\alpha t} = \bar{F}_\xi(\alpha - i\omega) \cdot \xi \tag{II-12}$$

so that comparing equations (II-9) and (II-12)

$$F_\xi(\alpha) = \bar{F}_\xi(\alpha - i\omega) \tag{II-13}$$

and the results expressed in eq. (D-6) follow.

In order to demonstrate the validity of eq. (D-8), apply eq. (II-3) to the upper left gradient of eq. (D-7), (omitting subscript (n))

$$\bar{F} = (\bar{X}_x + i\bar{Y}_x)x + (\bar{X}_y + i\bar{Y}_y)y \tag{II-14}$$

substitute

$$\left.\begin{aligned} x &= \frac{1}{2}(\bar{\xi} + \bar{\xi}^*) \\ y &= \frac{-i}{2}(\bar{\xi} - \bar{\xi}^*) \end{aligned}\right\} \tag{II-15}$$

where $\bar{\xi}^*$ = conjugate of $\bar{\xi}$.

$$\left.\begin{aligned} \bar{F} = {} & \frac{1}{2}\left[\bar{X}_x + \bar{Y}_y + i(\bar{Y}_x - \bar{X}_y)\right]\bar{\xi} \\ & + \frac{1}{2}\left[\bar{X}_x - \bar{Y}_y + i(\bar{Y}_x + \bar{X}_y)\right]\bar{\xi}^* \end{aligned}\right\} \tag{II-16}$$

Eq. (II-16) applies to a single blade. Let the advance angle of the jth blade with respect to the reference azimuth be $\psi_j = \frac{2\pi j}{n}$ where n is the number of blades. Then for a homogeneous input given by eq. (II-8),

$$\left.\begin{aligned} \xi_j &= \xi_o\, e^{(\alpha - i\omega t) - i\psi_j} \\ \xi_j^* &= \xi_o\, e^{(\alpha + i\omega t) + i\psi_j} \end{aligned}\right\} \qquad \text{(II-17)}$$

Combining (II-5), (II-16) and (II-17), the force on the hub in the stationary system due to a single blade is

$$F = \frac{1}{2}\left[\overline{X}_x + \overline{Y}_y + i(\overline{Y}_x - \overline{X}_y)\right]_{p=\alpha - i\omega} \cdot \xi_o\, e^{\alpha t} + \frac{1}{2}\left[\overline{X}_x - \overline{Y}_y + i(\overline{Y}_x + \overline{X}_y)\right]_{p=\alpha + i\omega} \cdot \xi_o\, e^{(\alpha + 2i\omega)t + 2i\psi_j} \qquad \text{(II-18)}$$

Now if the blades are symmetrically arranged with respect to the hub

$$\sum_{j=1}^{n} e^{2i\psi_j} = 0 \qquad \text{for } n \geq 3$$

Hence with the exception of single-bladed and two-bladed rotors, the net fore on the hub is:

$$F = \frac{n}{2}\left[\overline{X}_x + \overline{Y}_y + i(\overline{Y}_x - \overline{X}_y)\right]_{p=\alpha - i\omega} \xi_o\, e^{\alpha t} \qquad \text{(II-19)}$$

and the result expressed in eq. (D-8) follows. For one and two-bladed rotors it will be observed that, for $|\alpha| \ll \omega$, the additional terms in eq. (II-18) are sinusoids with frequency approximately equal to 2ω. Thus for low frequency calculations these additional terms have negligible influence.

APPENDIX III

Quantities Required in the Evaluation of Rotor Derivatives

For $\bar{p} = -i$

$$\overline{H}_{\xi\xi} = 0$$

$$\overline{H}_{\xi\eta} = -\overline{V}_t \frac{\ell_{11}^2}{\ell_{10}} \sin\beta_c \tan\beta_c - i\ell_{10}\sin\beta_c$$

$$\overline{H}_{\eta\xi} = 0$$

$$\overline{H}_{\eta\eta} = -b\ell_{01}\cos^3\beta_c + \sin^2\beta_c\left[b^2 + 2\ell_{02}^2 + \ell_{11}^2(1 - \cos\beta_c)\right] - i\,\frac{\overline{V}_t b\ell_{11}^2}{\ell_{10}}\sin\beta_c$$

$$\frac{d}{d\bar{p}}(\overline{H}_{\xi\xi}) = -\overline{V}_t \tan\beta_c \sin^2\beta_c$$

$$\frac{d}{d\bar{p}}(\overline{H}_{\xi\eta}) = i\overline{V}_t\, b\sin^2\beta_c$$

$$\frac{d}{d\bar{p}}(\overline{H}_{\eta\xi}) = -i\overline{V}_t\, b\sin^2\beta_c$$

$$\frac{d}{d\bar{p}}(\overline{H}_{\eta\eta}) = -\overline{V}_t b^2 \sin\beta_c\cos\beta_c + i(2b^2 + 2\ell_{02}^2)\sin^2\beta_c$$

$$H_x^* + iH_y^* = \overline{V}_t \frac{\ell_{11}^2}{\ell_{10}}\tan\beta_c + i\ell_{01}(2\tan\beta_c \sin\beta_c - \cos\beta_c)$$

$$H_\phi^* + iH_\theta^* = b\ell_{01}(\operatorname{ctn}\beta_c - 3\sin\beta_c) - 2\ell_{02}^2\sin\beta_c + i\overline{V}_t\,\frac{b\ell_{11}^2}{\ell_{10}}$$

$$B_x^* - iB_y^* = 0$$

$$B_\phi^* - iB_\theta^* = b\ell_{01}\operatorname{ctn}\beta_c - 2\ell_{02}^2\sin\beta_c + i\,\frac{\overline{V}_t}{\ell_{10}}\left[b\ell_{11}^2 - \ell_{21}^2 - \ell_{12}^3\sin\beta_c\tan\beta_c\right]$$

$$\frac{d}{d\bar{p}}(H_x^* + iH_y^*) = i\overline{V}_t\frac{\ell_{11}^2}{\ell_{10}}\tan\beta_c$$

$$\frac{d}{d\bar{p}}(H_\phi^* + iH_\theta^*) = -\overline{V}_t\frac{b\ell_{11}^2}{\ell_{10}} + i(2b\ell_{01}\operatorname{ctn}\beta_c - 2\ell_{02}^2\sin\beta_c)$$

$$\frac{d}{d\bar{p}}(B_x^* - iB_y^*) = -i\overline{V}_t\frac{\ell_{11}^2}{\ell_{10}}\tan\beta_c$$

$$\frac{d}{d\bar{p}}(B_\phi^* - iB_\theta^*) = -\overline{V}_t\frac{b\ell_{11}^2}{\ell_{10}} + i(2b\ell_{01}\operatorname{ctn}\beta_c - 2\ell_{02}^2\sin\beta_c)$$